Spatial competition of the ground states in 1111 iron pnictides

G. Lang,[1,2,*] L. Veyrat,[1] U. Gräfe,[1] F. Hammerath,[1,3] D. Paar,[1,4] G. Behr,[1] S. Wurmehl,[1,3] and H.-J. Grafe[1]

[1]*IFW Dresden, Institute for Solid State Research, PF 270116, D-01171 Dresden, Germany*

[2]*ESPCI ParisTech, PSL Research University; CNRS; Sorbonne Universités, UPMC Université Paris 6; LPEM, 10 rue Vauquelin, F-75231 Paris Cedex 5, France*

[3]*Institut für Festkörperphysik, Technische Universität Dresden, D-01062 Dresden, Germany*

[4]*Department of Physics, Faculty of Science, University of Zagreb, P.O. Box 331, HR-10002 Zagreb, Croatia*

(Received 26 August 2015; revised manuscript received 26 May 2016; published 20 July 2016)

Using nuclear quadrupole resonance, the phase diagram of 1111 $R\mathrm{FeAsO}_{1-x}\mathrm{F}_x$ (R = La, Ce, Sm) iron pnictides is constructed as a function of the local charge distribution in the paramagnetic state, which features low-doping-like (LD-like) and high-doping-like (HD-like) regions. Compounds based on magnetic rare earths (Ce, Sm) display a unified behavior, and comparison with La-based compounds reveals the detrimental role of static iron 3*d* magnetism on superconductivity, as well as a qualitatively different evolution of the latter at high doping. It is found that the LD-like regions fully account for the orthorhombicity of the system, and are thus the origin of any static iron magnetism. Orthorhombicity and static magnetism are not hindered by superconductivity but limited by dilution effects, in agreement with two-dimensional (2D) (respectively three-dimensional) nearest-neighbor square lattice site percolation when the rare earth is nonmagnetic (respectively magnetic). The LD-like regions are not intrinsically supportive of superconductivity, contrary to the HD-like regions, as evidenced by the well-defined Uemura relation between the superconducting transition temperature and the superfluid density when accounting for the proximity effect. This leads us to propose a complete description of the interplay of ground states in 1111 pnictides, where nanoscopic regions compete to establish the ground state through suppression of superconductivity by static magnetism, and extension of superconductivity by proximity effect.

DOI: 10.1103/PhysRevB.94.014514

I. INTRODUCTION

One of the main motivations to study iron-based high-temperature superconductors (IBSs) is the frequent vicinity of unconventional superconductivity and static magnetism in their phase diagram. Also observed in copper-based superconductors, it raises the questions of ground-state interplay and of the role of spin fluctuations in the Cooper pairing interaction. By applying pressure, changing the doping, or altering the electronic structure via isovalent substitutions [1,2], the ground state of most IBSs can be modified from static magnetism towards superconductivity, with the possibility of ground-state coexistence on a microscopic scale in several cases [3–10].

A key aspect of iron-based superconductors is the itinerant, multiband character of their electronic structure. In compounds such as the 1111 and 122 families, the low-temperature magnetic order of the parent compounds ($T_N \approx 140$ K for the 1111 family) is argued to be a spin-density wave caused by the nesting properties of the Fermi surface [11,12]. As this transition is associated to a tetragonal-to-orthorhombic structural transition at the same or a slightly higher temperature, both Ising-nematic spin fluctuations and orbital fluctuations have been invoked to explain the observed anisotropic electronic response of the iron plane above the magnetic transition [13]. Evolutions of the Fermi surface with doping would affect the competition of ground states, and relative changes in interband and intraband scattering would play a role in determining whether superconductivity is associated to spin or orbital fluctuations, yielding respectively a $s\pm$ or s_{++} symmetry of the order parameter [14–17].

The ground-state competition is, however, complicated by spatial electronic inhomogeneities which derive either from the local effect of in-plane chemical substitutions [18–20], or from intrinsic iron plane physics. Using nuclear quadrupole resonance (NQR), a local probe of the charge environment, we have previously shown that the fluorine-doped 1111 family ($R\mathrm{FeAsO}_{1-x}\mathrm{F}_x$ with R a rare earth) features two types of local electronic environments intrinsic to the FeAs layers when moderately doped [21]. Although these environments are already defined in the paramagnetic state, their simultaneous presence in purely magnetic or purely superconducting samples appears to rule out a trivial explanation of any ground-state coexistence in 1111 compounds. Further complicating the analysis of ground-state interplay, such coexistence seems dependent on the choice of rare earth (La, Ce, Sm...) [3,22]. Obscuring the whole phase diagram is the difficulty in assessing the true doping, which may differ dramatically from the nominal doping depending on the rare earth and the synthesis route [23–25].

In this paper, we present how the nanoscale charge environments observed by NQR in the paramagnetic state yield a highly accurate determination of the effective doping, allowing us to compare unambiguously the phase diagrams of $R\mathrm{FeAsO}_{1-x}\mathrm{F}_x$ (R = La, Ce, Sm) and to explain the evolution of ground-state properties with doping. Section III describes how to obtain such phase diagrams, which are found undistinguishable for the two magnetic rare earths (Ce, Sm). The different behavior for lanthanum shows that static magnetism from the iron has a detrimental effect on superconductivity, while at high doping La-based samples display a specific, nonmonotonous behavior of the superconducting transition temperature. In Sec. IV, it is found that the low-doping-like regions seen by NQR fully account for

*guillaume.lang@espci.fr

the orthorhombicity and iron static magnetism of the system. Nearest-neighbor square lattice percolation is at play, with dimensionality being dependent on whether the rare earth itself is magnetic. In Sec. V, it is shown that the low-doping-like regions can only host superconductivity by proximity, with intrinsic superconductivity originating from the high-doping-like regions seen by NQR. Finally, we propose in Sec. VI a full description of the interplay of ground states in 1111 pnictides, where superconductivity extends spatially whenever static magnetism is weak enough in the nearby microscopic regions.

II. EXPERIMENTAL DETAILS

Two different routes were followed for the synthesis of the polycrystalline $R\mathrm{FeAsO}_{1-x}\mathrm{F}_x$ (R = La, Ce, Sm) samples. For route 1, FeAs was prepared by a solid-state reaction prior to the synthesis of the corresponding 1111 compounds. Subsequently, the resulting FeAs was mixed with metallic R, R_2O_3, and RF_3 in a stoichiometric ratio. This mixture was homogenized by grinding in a mortar. For route 2, we prepared RAs as first step by reacting R and As lumps in a stoichiometric ratio via a vapor transport reaction. The second step of route 2 used the resulting RAs, Fe, Fe_2O_3, and FeF_3 as starting materials in a stoichiometric ratio. Here, the starting materials were homogenized by grinding in a ball mill. In either case, the resulting powders were pressed into pellets under Ar atmosphere, and subsequently annealed in an evacuated quartz tube in a two-step synthesis first at 940 °C for 12 h and then at 1150 °C for up to 60 h. All samples were characterized by powder x-ray diffraction (XRD) and by scanning electron microscopy (SEM) with semiquantitative elemental analysis using the wavelength dispersive x-ray (WDX) mode. Their structural properties and their structural, magnetic, and superconducting phase transitions were determined using a wide array of techniques: standard XRD, synchrotron XRD at low temperature, magnetic susceptibility, electrical resistivity, muon spin relaxation and rotation (μSR), Mössbauer spectroscopy, and nuclear magnetic resonance (NMR) [22,26–30]. The determination of the doping will be discussed in the next section, with all phase transitions being included in Fig. 4.

In order to probe the distribution of charge environments at the nanometer scale, ^{75}As nuclear quadrupole resonance (NQR) was used. NQR probes nuclei with spin $I > 1/2$, which possess a finite electric quadrupole moment eQ with e the elementary charge and Q the nuclear quadrupole moment. In the absence of applied or internal magnetic field, any finite electric-field gradient (EFG) at the atomic site will lift at least partially the degeneracy of the nuclear electric quadrupole energy levels, according to the following Hamiltonian [31]:

$$\mathcal{H} = \frac{eQV_{zz}}{4I(2I-1)}\left[3I_z^2 - I(I+1) + \frac{\eta}{2}(I_+^2 + I_-^2)\right], \quad (1)$$

whose coordinate axes are defined by the principal axes of the electric-field gradient (EFG) tensor, itself characterized by its largest principal value V_{zz} and its asymmetry parameter $\eta = (V_{xx} - V_{yy})/V_{zz}$ ($|V_{zz}| \geqslant |V_{yy}| \geqslant |V_{xx}|$ and $0 \leqslant \eta \leqslant 1$). Since ^{75}As has a nuclear spin $I = 3/2$, the Hamiltonian yields a single resonance frequency:

$$\nu_Q = \frac{eQV_{zz}}{2h}\sqrt{1 + \frac{\eta^2}{3}}, \quad (2)$$

where h is Planck's constant. The electric quadrupole frequency ν_Q depends on the symmetry and amplitude of the EFG, which itself depends on the atomic/nanoscale charge environment. For every local charge environment as seen from the arsenic sites, one resonance line will be observed.

Using a standard pulsed NQR spectrometer, radio-frequency irradiations over a typical ν_{rf} = 8–14-MHz frequency range were performed to obtain the histogram of resonance frequencies for all arsenic sites in the sample. Powder samples were crushed to ensure that the crystallites are small enough to obtain a good penetration of the radio-frequency field. Note that operating on powders does not affect the spectra, since $\mathcal{H}$ depends on the principal axes of the local EFG, i.e., the resonance frequency for a given charge environment is independent of the orientation of individual crystallites. Spin-echo sequences ($\frac{\pi}{2}$-τ-π) were used, with typical τ = 20–30 μs. The τ values and the pulse sequence repetition rates were checked to be small enough that spin-spin or spin-lattice relaxation contrast do not distort the relative line intensities. Point-by-point spectra were obtained by integrating the full echo and applying a ν_{rf}^{-2} intensity correction.

III. RECONSTRUCTED PHASE DIAGRAM

In most of the published literature, nominal dopings are used to build the phase diagrams of iron-based superconductors. While this yields qualitatively correct results for a given sample series, it is known that the real doping may be significantly lower, especially for high nominal dopings [23–25]. It is thus difficult to extract quantitative information (e.g., doping thresholds), and to compare different compounds in terms of ground-state competition and the doping profile of the superconductivity dome. For F-doped 1111 compounds, real content determination using WDX spectroscopy is hardly possible for cerium-based compounds due to the superposition of the relevant Ce and F lines, and may generally be affected by the presence of poorly crystallized impurities which XRD cannot easily account for. Using fluorine NMR, the doping could be established within an absolute error of 2% [6,32], which is satisfactory for high dopings but may be imprecise to discuss the boundary between the two ground states at low doping. Here, we propose to take advantage of the doping dependence of the charge environments previously seen by NQR for La- and Sm-based samples [21].

A. Principle

Figure 1 shows the NQR spectra for R-1111 (R = La, Ce, Sm) in the paramagnetic state over a broad doping range (itself determined by NQR as described below, see also Table I for the fluorine content). Whereas undoped and highly doped samples display a single peak corresponding to a single charge environment, the samples at intermediate doping display two peaks (two charge environments) which were shown to correspond to a nanoscale electronic inhomogeneity intrinsic to the FeAs layers [21]. Defining ν_Q^L (ν_Q^H) and w^L

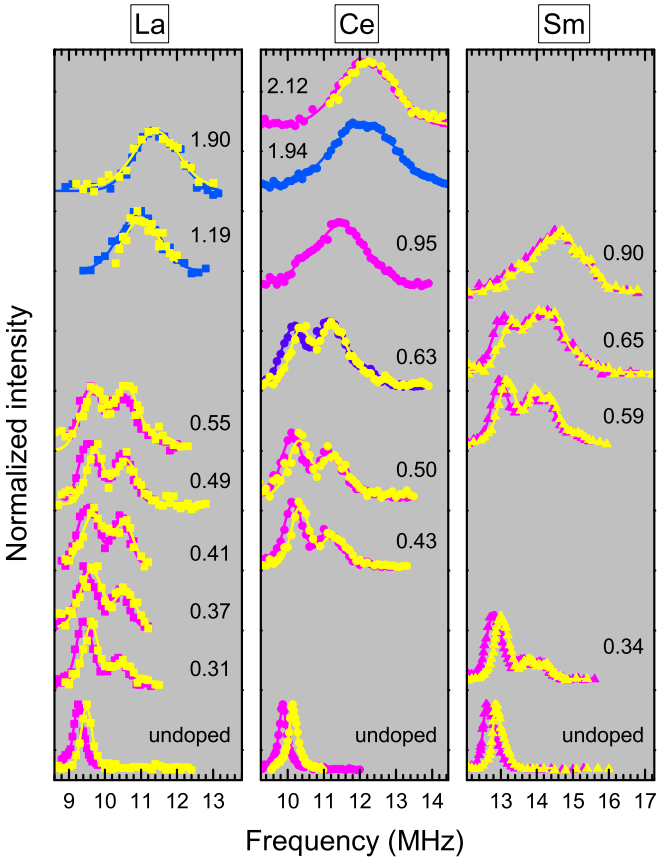

FIG. 1. NQR spectra of the studied samples in the paramagnetic state. The doping is indicated as $x_{\mathrm{NQR}}/x_{\mathrm{FSWT}}$ (FSWT: full spectral weight transfer; see text). The measurement temperature is coded by the color (see also the scale in Fig. 3): Yellow for room temperature, magenta for 150–160 K, indigo for 100 K (Ce, $x_{\mathrm{NQR}}/x_{\mathrm{FSWT}} = 0.63$), blue for 40–55 K. Full lines are Gaussian fits. Some low-temperature La/Sm spectra are from a previous study [21].

(w^H) as the low-frequency (high-frequency) peak's position and spectral weight ($w^L + w^H = 1$), and x as the WDX-established doping, these two charge environments were found to have the following properties: (i) the transfer of spectral weight is linear with x and is completed ($w^L = 0$) at $x \approx 0.1$; (ii) ν_Q^L and ν_Q^H vary linearly with x, extrapolating respectively to the frequencies of the $x = 0$ and $x = 0.1$ charge environments; (iii) the linear x dependence of ν_Q^H appeared to extend beyond $x = 0.1$, which was independently confirmed [33]. The low- and high-frequency peaks were thus associated to low-doping-like (LD-like) and high-doping-like (HD-like) regions. This choice of name reflects that it cannot be ruled out that the electronic differences are due to the orbital degree of freedom, rather than the charge degree of freedom [21]. Note that the doping dependence of ν_Q is expected to come from a change in the local electronic distribution, rather than from changes in the lattice parameters [34].

Taking advantage of the fact that NQR is immune to spurious phases and allows us to measure with good precision the peak positions and the spectral weights in practically all samples, we reverse the above observations to define x_{NQR}, a NQR-defined doping. For samples with *doping low enough that two charge environments are observed*, following point (i) we set

$$x_{\mathrm{NQR}} = w^H x_{\mathrm{FSWT}}, \tag{3}$$

with x_{FSWT} the value for which full spectral weight transfer (FSWT) has occurred, i.e., the electronic homogeneity is restored. For samples with *doping large enough that a single charge environment is observed* ($w^H = 1$), following point (iii) we set x_{NQR} such that ν_Q^H is linear versus this variable.

TABLE I. Doping information on the samples from this study, as well as on samples from previous $LaO_{1-x}F_xFeAs$ NQR/NMR studies whose spectral properties have been re-analyzed following the same procedure as for our samples. R indicates the rare earth. For samples from the literature, the name of the first author is given next to the reference number. x indicates the fluorine doping. For our La-based samples it is the nominal value, which is on the order of the WDX value, whereas for our Sm-based samples it is a rescaled value derived from WDX measurements [26,27]. For our Ce samples it is the nominal value, without the possibility of comparison to WDX values due to the superposition of the relevant Ce and F lines. For samples from the literature it is usually the nominal value. $x_{\mathrm{NQR}}/x_{\mathrm{FSWT}}$ is the NQR-derived doping as defined in Sec. III A. x_{FSWT} is the per-sample extrapolated fluorine content for which full spectral weight transfer would occur in the NQR spectrum (see Sec. III C).

R	Source	x	$x_{\mathrm{NQR}}/x_{\mathrm{FSWT}}$	x_{FSWT}
La	this study	0	0.00	
		0.035	0.31(4)	0.11
		0.04	0.37(4)	0.11
		0.045	0.41(2)	0.11
		0.05	0.49(4)	0.10
		0.075	0.55(3)	0.14
		0.1	1.19(6)	0.08
		0.15	1.90(2)	0.08
Ce	this study	0	0.00	
		0.05	0.43(2)	0.12
		0.15	0.50(2)	0.30
		0.1	0.63(2)	0.16
		0.1	0.95	0.11
		0.2	1.94	0.10
		0.25	2.12(7)	0.12
Sm	this study	0	0.00	
		0.04	0.34(2)	0.12
		0.06	0.59(2)	0.10
		0.08	0.65(4)	0.12
		0.1	0.90(4)	0.11
La	[35] - Kitagawa	0.14	1.98	0.07
	[33] - Oka	0.03	0.40(4)	0.07
		0.04	0.48(4)	0.08
		0.06	0.90(5)	0.07
		0.08	1.09	0.07
		0.1	1.67	0.06
		0.15	2.64(8)	0.06
	[36] - Tatsumi	0.14	1.51	0.09
	[37] - Mukuda	0.22	2.03(22)	0.11
	[38] - Kobayashi	0.11	0.56(5)	0.20
		0.15	1.33	0.11
	[39] - Nitta	0.14	1.80(27)	0.08

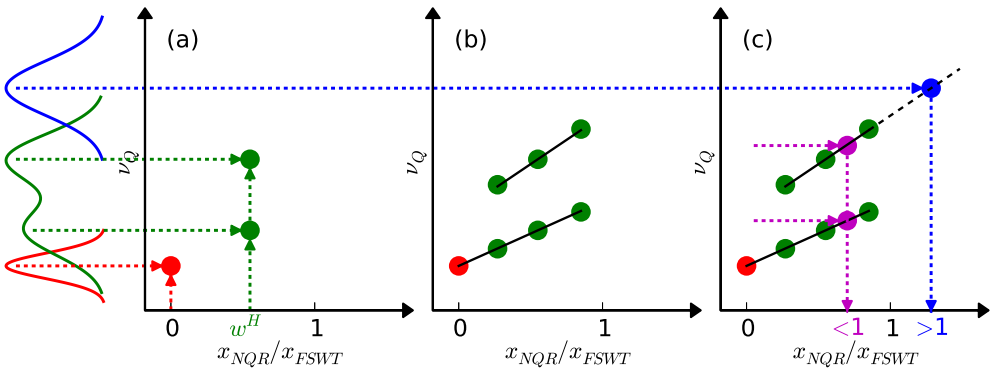

FIG. 2. Procedure to extract $x_{\mathrm{NQR}}/x_{\mathrm{FSWT}}$ for a sample with high-enough doping that a single NQR line is present, or for a sample with two NQR lines of uncertain relative weights. See the main text for details. Computer-generated data are used. Typical spectral shapes are shown on the left side. (a) Construction of ν_Q as a function of $x_{\mathrm{NQR}}/x_{\mathrm{FSWT}} = w^H$. (b) Linear fits of the two frequency branches. (c) Extraction of $x_{\mathrm{NQR}}/x_{\mathrm{FSWT}}$ knowing ν_Q.

While it seems from point (i) that x_{FSWT} corresponds to about 10% fluorine content, we will show later that this value cannot be estimated very precisely and that it is more reliable to express x_{NQR} in units of x_{FSWT} (i.e., to determine the ratio $x_{\mathrm{NQR}}/x_{\mathrm{FSWT}}$) rather than as a fluorine-content equivalent doping. Therefore, for samples with doping low enough that two NQR lines are present we use $x_{\mathrm{NQR}}/x_{\mathrm{FSWT}} = w^H$. For samples with doping high enough that a single NQR line is present the following procedure is applied (see Fig. 2): (a) for every sample with two NQR lines (green spectrum), the two ν_Q values are plotted versus $x_{\mathrm{NQR}}/x_{\mathrm{FSWT}} = w^H$. The single ν_Q value of the undoped compound (red spectrum) can be trivially added ($x_{\mathrm{NQR}}/x_{\mathrm{FSWT}} = 0$). (b) The two frequency branches are linearly fitted (full black lines). (c) The high-doping extrapolation (dashed black line) of the high-frequency branch allows us to extract the $x_{\mathrm{NQR}}/x_{\mathrm{FSWT}}$ value (“>1”) of the highly doped, single-peaked spectrum (blue spectrum). Note that the two linear fits also allow us to extract $x_{\mathrm{NQR}}/x_{\mathrm{FSWT}}$ (“<1”) for a sample whose peak frequencies are well known (purple points) but the w^H spectral weight less so.

B. Data extraction

From all measured spectra and using the above procedure to determine $x_{\mathrm{NQR}}/x_{\mathrm{FSWT}}$, we obtain Fig. 3. While complicated by the presence of multiple rare earths and measurement temperatures, as well as additional frequency branches, this figure is fundamentally the same as the final panel of Fig. 2. The vertical axes are offset so that there is overlap for all three rare earths at $x_{\mathrm{NQR}} = 0$ and room temperature. Such overlap is preserved for the whole ν_Q^L low-frequency branch (“L”) at room temperature, with a well-defined linear dependence on x_{NQR} (yellow fits) as expected from the above points (i) and (ii). This linear behavior holds against changes in temperature, albeit with different slopes for the different rare earths (purple fits for $T \approx 160$ K). The influence of temperature will be considered when discussing orthorhombicity and static magnetism in Sec. IV. For the ν_Q^H high-frequency branch with $x_{\mathrm{NQR}} < x_{\mathrm{FSWT}}$, the situation is complicated by the presence of a superstructure in the high-frequency peak of the Sm samples, which appears to be partially echoed in the $x_{\mathrm{NQR}}/x_{\mathrm{FSWT}} = 0.55$ La sample and $x_{\mathrm{NQR}}/x_{\mathrm{FSWT}} = 0.63$ Ce sample, thus a total of three high-frequency branches (“$H_1/H_2/H_3$”). Nonetheless, similar linear behaviors account well for the data (see yellow and purple fits). For the samples with $x_{\mathrm{NQR}} > x_{\mathrm{FSWT}}$, i.e., only La- or Ce-based samples, we apply the above procedure of extrapolating the linear behavior at $x_{\mathrm{NQR}} < x_{\mathrm{FSWT}}$. The H_1 frequency branch is used, since the H_2 and H_3 branches appear to play little to no role for La- and Ce-based samples. Note that this may not hold true for Sm-based samples (no sufficiently highly doped samples were available to test for this). Since at high doping the temperature dependence of the spectra vanishes (La) or is much reduced (Ce), we use a single extrapolation intermediate between the low-temperature (La, Ce) and room-temperature (La) H_1 fits (no reliable room-temperature H_1 fit is available for Ce, but the corresponding data are roughly similar to the La data). This interpolation is shown as a dashed line in Fig. 3.

The procedure to determine $x_{\mathrm{NQR}}/x_{\mathrm{FSWT}}$ was also applied to $LaO_{1-x}F_xFeAs$ NQR/NMR data from the literature (Refs. [33,35–39]). All included samples are listed in Table I together with their $x_{\mathrm{NQR}}/x_{\mathrm{FSWT}}$ value. In the following, they are designated as “*source-x*,” where *source* is the first author of the original paper and x is the reported fluorine content. In most cases, the availability of the NQR spectra allowed us to reanalyze them in the same way as for our own samples. A few samples for which data were too sparse or fit anomalies were present are excluded. For the samples with two-peaked spectra (Oka-0.03, Oka-0.04, and Kobayashi-0.11), the spectral weights obtained from the fits yield $x_{\mathrm{NQR}}/x_{\mathrm{FSWT}}$ values respectively equal to 0.40(4), 0.57(2), and 0.56(5). However, the reliability of these values may be affected by the experimental conditions under which the spectra were measured, i.e., the radio-frequency pulse sequence repetition time and the delay τ between the pulses (see Sec. II). If the former is too short or the latter too long, the relative spectral weights will be modified due to differences in T_1 (spin-lattice relaxation time) or T_2 (spin-spin relaxation time) between the two peaks [21]. This may be the case for the Oka-0.06 sample, whose single NQR peak’s frequency implies $x_{\mathrm{NQR}}/x_{\mathrm{FSWT}} = 0.90(5)$, i.e., a value for which two peaks should be observed. Here, the expected low-frequency peak may be entirely missed due to its small weight [10(5)%] being further reduced by so-called T_2 relaxation contrast. Note that the spectral linewidth for

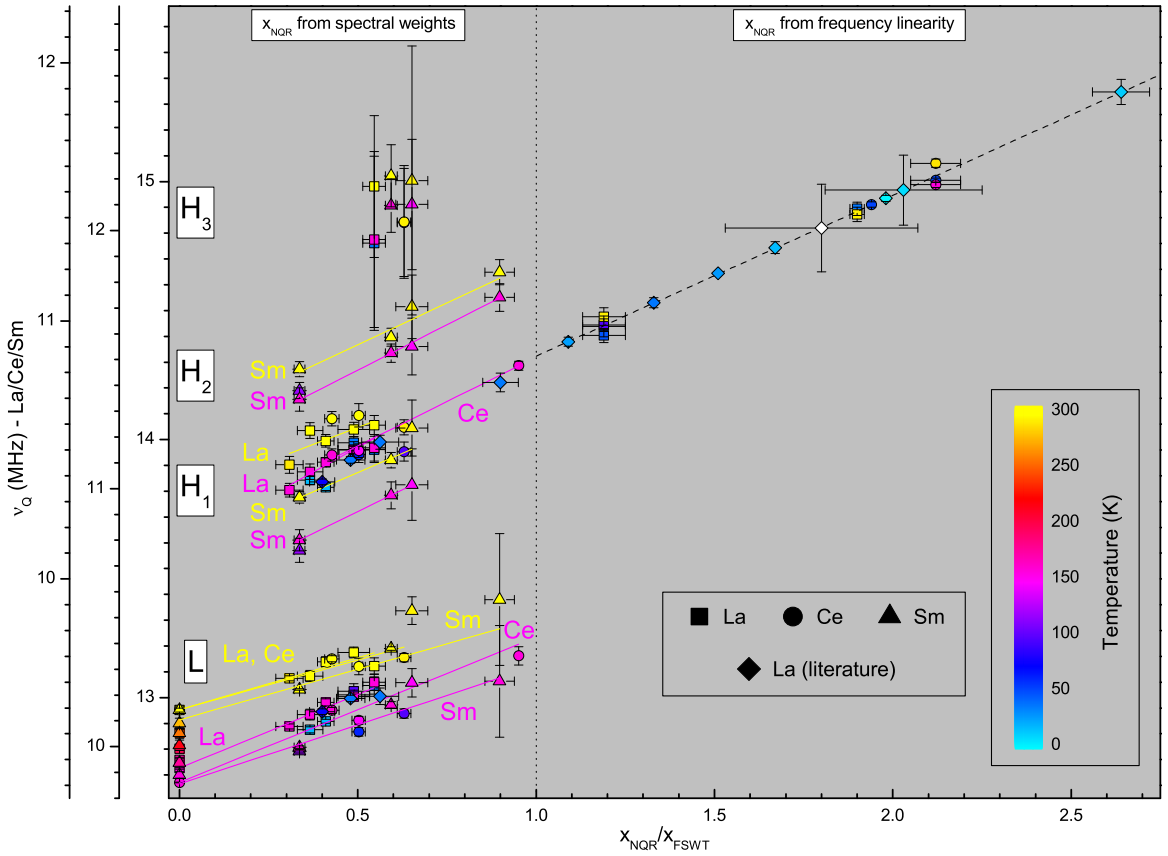

FIG. 3. Quadrupolar frequency vs $x_{\mathrm{NQR}}/x_{\mathrm{FSWT}}$. The L/$H_1$/$H_2$/$H_3$ labels refer to the observed frequency branches. Literature data are taken from Refs. [33,35–39] (for one sample, the unknown measurement temperature is color coded as white). For $x_{\mathrm{NQR}}/x_{\mathrm{FSWT}} < 1$, x_{NQR} is determined using the NQR spectral weights (see text for comments about some samples from Ref. [33]). Linear fits are indicated as full lines with attached labels. For each sample, the error on x_{NQR} is derived from fits of the spectra at one or more temperatures. For $x_{\mathrm{NQR}}/x_{\mathrm{FSWT}} > 1$, x_{NQR} is determined from the linear extrapolation of the low x_{NQR} behavior, indicated as a dashed line (when multiple measurement temperatures are available for a single sample, the small variations of ν_Q are accounted for by the horizontal error bars intercepting the dashed line). For each sample, the error on x_{NQR} is set so as to account for the uncertainty on ν_Q, whether experimental on a single point or due to remaining temperature dependence.

this sample is comparable to that of the high-frequency peaks of our $0 < x_{\mathrm{NQR}}/x_{\mathrm{FSWT}} < 1$ La samples, and lower than that of our $x_{\mathrm{NQR}}/x_{\mathrm{FSWT}} = 1.19$ La sample, in agreement with the determined $x_{\mathrm{NQR}}/x_{\mathrm{FSWT}}$. Considering the resonance frequencies obtained from the fits, the above $x_{\mathrm{NQR}}/x_{\mathrm{FSWT}}$ values for Oka-0.03 and Kobayashi-0.11 appear reasonably compatible with the L and H_1 frequency branches defined by our samples (see the corresponding diamond symbols in Fig. 3). For Oka-0.04, the agreement is somewhat poorer and suggests that the actual $x_{\mathrm{NQR}}/x_{\mathrm{FSWT}}$ value is lower than the fit-derived value of 0.57(2). This is supported by the comparison of spin-lattice relaxation rate measurements in Refs. [33] and [21], showing that Oka-0.04 is indeed rather lower doped than our 5% fluorine sample for which $x_{\mathrm{NQR}}/x_{\mathrm{FSWT}} = 0.49(4)$. Based on agreement with the L and H_1 frequency branches, $x_{\mathrm{NQR}}/x_{\mathrm{FSWT}}$ is then estimated to be 0.48(4), as used in Fig. 3.

C. Estimation of x_{FSWT}

All obtained $x_{\mathrm{NQR}}/x_{\mathrm{FSWT}}$ values are reported in Table I. To get an estimate of x_{FSWT}, one can compute $x(x_{\mathrm{NQR}}/x_{\mathrm{FSWT}})^{-1}$ for every sample: by setting $x_{\mathrm{NQR}} = x$ (the nominal/reported fluorine content of the sample), x_{FSWT} will be the fluorine content for which full NQR spectral weight transfer would occur in a given sample, *with an inaccuracy corresponding to that present in* x. As can be seen in Table I most computed values of x_{FSWT} are in the range 0.06–0.12, while a few values are slightly (0.14, 0.16) or much (0.20, 0.30) higher. The most likely candidate for this variability is fluorine that did not enter the matrix 1111 phase (pushing x_{FSWT} up for a given sample), although other sources cannot be ruled out (e.g., small amounts of oxygen or arsenic vacancies which might drive down x_{FSWT}). This variability plays however no role in our study, where all deductions will be made on the basis of the $x_{\mathrm{NQR}}/x_{\mathrm{FSWT}}$ ratio, which does not depend on any chemical characterization.

D. Phase diagram

The phase diagram for all three rare earths is rebuilt in a systematic way as a function of $x_{\mathrm{NQR}}/x_{\mathrm{FSWT}}$, as shown on Fig. 4. The characterization of our samples is taken almost exclusively from Refs. [22,26–30], in particular the work of Maeter *et al.* where first estimates of x_{NQR} were used for Ce-based samples. For samples from the literature, the transition temperatures are taken from the original papers. For a given technique, the data were harmonized whenever possible

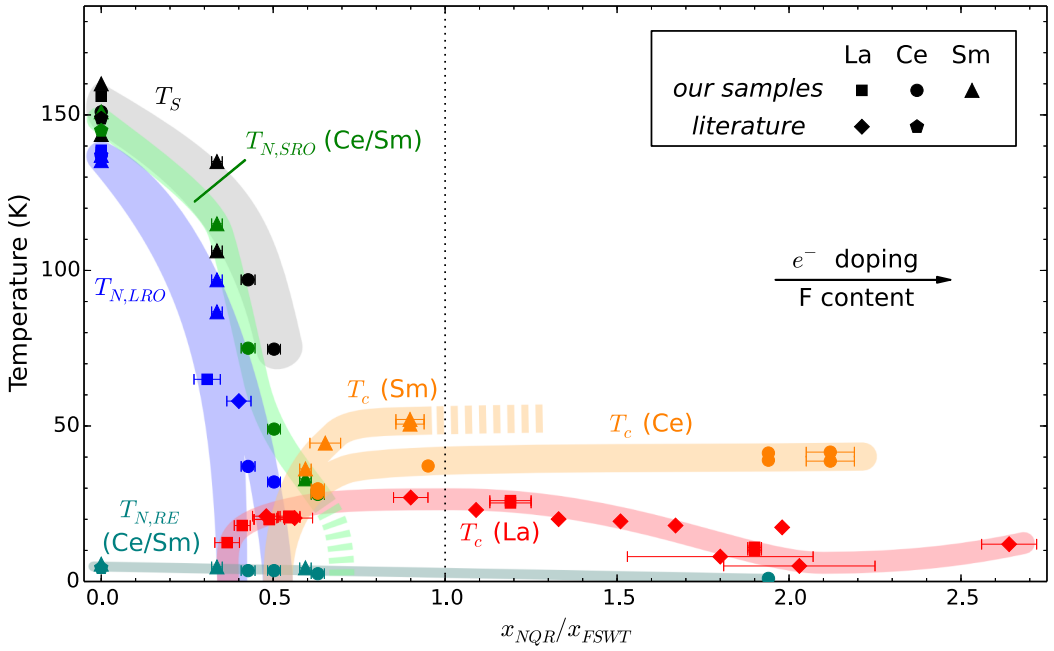

FIG. 4. Phase diagram of $R\mathrm{FeAsO}_{1-x}\mathrm{F}_x$ (R = La, Ce, Sm) as a function of $x_{\mathrm{NQR}}/x_{\mathrm{FSWT}}$. For some samples and some transitions, more than one point may be displayed due to characterization using multiple techniques. The samples from the literature are referenced in Table I, except the undoped Ce-based sample from Ref. [29]. The broad lines are visual guides.

by extracting the transition temperature in a systematic way (e.g., midpoint of the resistivity drop for the superconducting transition). In any case, the use of different techniques for a given phase transition necessarily yields some additional point dispersion, which is taken into account by the visual guides of Fig. 4. The transition lines are well defined, which shows the adequacy of our NQR approach to the doping. This is especially true for La-based compounds, with twelve samples from other NQR groups with different sample sources being successfully combined to our eight samples.

The tetragonal-to-orthorhombic structural transition and the transition to long-range-ordered (LRO) magnetism can be described by single T_S and $T_{N,\mathrm{LRO}}$ lines for cerium and samarium. In between these two transitions, a single $T_{N,\mathrm{SRO}}$ line describes the transition to short-range-ordered (SRO) magnetism, which extends slightly into the superconductivity region. Superconductivity appears about the same doping threshold for Ce and Sm, with the overall difference in T_c values reflecting the difference in maximal transition temperatures (43 K for Ce, 55 K for Sm) [29,40]. While no data are available for highly doped Sm-based samples, this suggests that the superconducting regions for Ce and Sm are similar, with maximal T_c being reached only at dopings far above the range where static magnetism and superconductivity meet. Finally, static magnetism of the rare earths also extends beyond this range. Thus, the phase diagrams for these two magnetic rare earths are highly similar.

In the case of lanthanum, several differences occur. $T_{N,\mathrm{LRO}}$ would appear to decrease faster: while few samples show this transition, there are several low-doped superconducting samples which do not show it, therefore constraining it to below $x_{\mathrm{NQR}}/x_{\mathrm{FSWT}} \approx 0.4$. SRO magnetism is completely absent from superconducting samples, although it cannot be ruled out in magnetic samples as a precursor of the LRO magnetic transition. Finally, the superconductivity region starts at lower doping and grows only until $x_{\mathrm{NQR}}/x_{\mathrm{FSWT}} \approx 1$, after which it decreases with a sign of recovery only at very high doping. A candidate for the difference in static magnetism compared to the unified behavior of Ce- and Sm-based samples is the lack of magnetism of lanthanum, whose formal 3+ charge implies closed electronic shells. This is verified experimentally by spin-lattice relaxation rate measurements: the spin fluctuations in La-based samples are much smaller (as well as more doping dependent) than in samples containing a magnetic rare earth (Ce, Sm, Nd), and are thus ascribed to iron plane magnetism for the former and to $4f$ rare-earth magnetism for the latter [21,41–44]. Static magnetism in the iron planes may thus be promoted at higher doping by magnetic rare earths (to be discussed in Sec. IV), and the concomitant delaying of superconductivity is a strong indication that static magnetism is detrimental to superconductivity. Regarding superconductivity at high fluorine doping in La-based samples, while it was already known that T_c tends to decrease [27], our phase diagram shows the indication of eventual T_c recovery. This is compatible with observations on hydrogen-doped samples [45]: a second superconductivity dome occurs for La at high doping, whereas for Ce and Sm there is a single dome extending to more than 40% doping. This difference is then argued to be related to the doping dependence of the iron $3d$ orbital degeneracy.

Note that the "ribbons" of Fig. 4 should be seen as an interval of confidence for each transition line. Especially, the $T \to 0$ superposition of the magnetic and superconducting phase transitions about $x_{\mathrm{NQR}}/x_{\mathrm{FSWT}} \approx 0.4$ (La) and ≈ 0.5 (Ce, Sm) should not be understood as a suggestion of a quantum critical point, whose relevance is anyhow unclear in

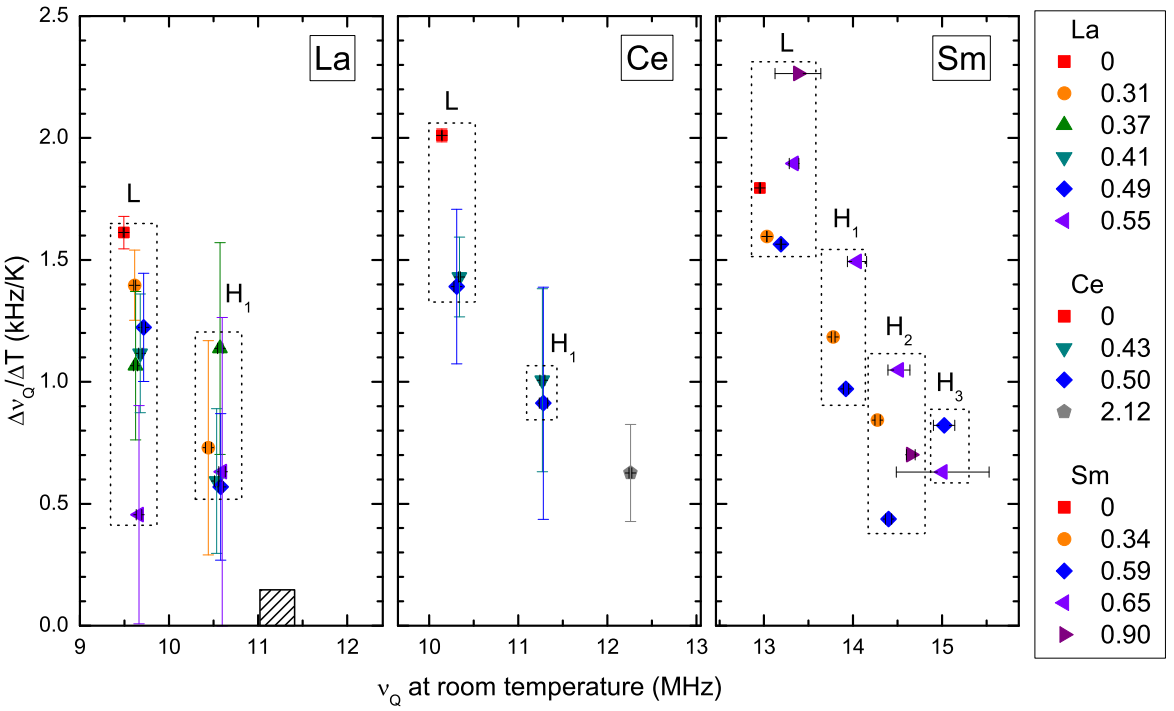

FIG. 5. Temperature sensitivity of the quadrupolar frequency, as a function of the peak position at room temperature. $\Delta\nu_Q/\Delta T$ is calculated from measurements at room temperature and at $T = 150$–160 K. The legend indicates $x_{\mathrm{NQR}}/x_{\mathrm{FSWT}}$. For $x_{\mathrm{NQR}} < x_{\mathrm{FSWT}}$, each dotted box groups the points belonging to the same frequency branch (L, H_1, H_2, H_3) as defined in Fig. 3. For La-based samples, the hatched rectangle about $\nu_Q \approx 11.2$ MHz indicates the frequency range over which $\Delta\nu_Q/\Delta T$ goes from weak ($x_{\mathrm{NQR}}/x_{\mathrm{FSWT}} = 1.19$) to zero or negative ($x_{\mathrm{NQR}}/x_{\mathrm{FSWT}} = 1.90$). Error bars for the Sm-based samples are not shown, as they exceed the actual point dispersion for each frequency branch, suggesting overestimation due to more complex spectra.

an inhomogeneous context. There may be a crossing of the two transitions lines, which must however be very limited in doping range considering that no sample is known to feature both long-range magnetic order and superconductivity. This will be discussed in terms of ground-state competition in Sec. VI.

Considering the electronic separation into regions which seem related either to the magnetically ordered, undoped compound or to the superconducting-only $x_{\mathrm{NQR}}/x_{\mathrm{FSWT}} = 1$ compound (see Fig. 3), it is a distinct possibility that these regions are respectively more prone to develop static magnetism or superconductivity. Taking into account our observations about the phase diagram and the fact that most samples exhibit only one of the two ground states, we examine this issue in the next two sections.

IV. ORTHORHOMBICITY AND STATIC MAGNETISM

A. Spatial origin

As shown on Figs. 1 and 3, the spectra in the paramagnetic state display a sizable temperature dependence for most of the samples, with an increase of the resonance frequency when increasing the temperature. The effect is largest for the undoped samples, and appears reduced or even canceled for single-peaked spectra at high doping, such as for the $x_{\mathrm{NQR}}/x_{\mathrm{FSWT}} = 1.90$ La-based sample. When the spectrum features two peaks, the temperature dependence of the high-frequency peak seems to be lower than that of the low-frequency peak, as can be seen for instance for the $x_{\mathrm{NQR}}/x_{\mathrm{FSWT}} = 0.65$ Sm-based sample. An increase of ν_Q with increasing temperature is also observed in other iron pnictides [46,47], and goes counter to the expected effect of lattice expansion and lattice vibrations [48]. This suggests that other changes take place with temperature, for instance intracell atomic displacements, which are beyond the scope of the present study and are left as an open question.

In the following, we focus on the $T \approx 160$–300-K range, i.e., a temperature range above all low-temperature transitions. Using the data plotted in Fig. 3, the ratio $\Delta\nu_Q/\Delta T$ is extracted for all spectral peaks of all samples over this temperature range. It is then plotted on Fig. 5 versus the resonance frequency of each corresponding peak at room temperature, i.e., as far away as possible from low-temperature physics. Such an abscissa allows us to reflect the frequency branch structure of Fig. 3 (see dotted boxes in Fig. 5). While the uncertainty on $\Delta\nu_Q/\Delta T$ for a given peak (a single point) is large, for a given rare earth the peaks belonging to the same branch feature a dispersion in $\Delta\nu_Q/\Delta T$ which is small enough to differentiate the various frequency branches, especially for Ce- and Sm-based samples. The tendency is for $\Delta\nu_Q/\Delta T$ to decrease when going from the L frequency branch to the H_1 branch (and then to the H_2/H_3 branches for Sm-based samples), whereas for a given branch large differences in the doping and low-temperature properties of the samples appear to be of lesser importance. This shows that the temperature dependence of the electronic charge environment at each arsenic site is a local electronic property, rather than an emergent property of the whole sample at a given overall doping. Note how this is different to previously obtained $1/T_1$ spin-lattice relaxation

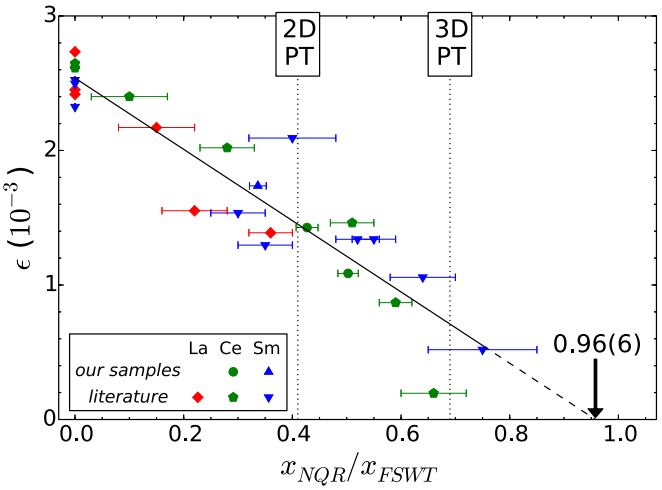

FIG. 6. Order parameter of the structural phase transition $\epsilon = (a-b)/(a+b)$ (a,b: in-plane lattice parameters) as a function of doping. The structural data for all samples are taken from Refs. [29,49–54]. The full line is a linear fit, with the dotted line showing its extrapolation to $\epsilon = 0$. Vertical dashed lines indicate the percolation thresholds for two- and three-dimensional (2D, 3D) nearest-neighbor square-lattice site percolation.

rate measurements on La-based samples [21], which showed a large doping dependence for both L- and H-branch sites. We ascribe this difference to ν_Q being sensitive to the charge degree of freedom (a defined configuration of $3d$ orbital occupancies) and to $1/T_1$ probing the spin degree of freedom (doping-dependent magnetic fluctuations).

The fact that the local electronic properties of the undoped, magnetically ordered compound are well retained across the L frequency branch suggests that the low-frequency regions may play the key role in establishing orthorhombicity and static magnetism, whereas the high-frequency regions may play no role at all. To test this hypothesis, the order parameter $\epsilon = (a-b)/(a+b)$ (a,b: in-plane lattice parameters) of the structural transition is plotted as a function of $x_{\mathrm{NQR}}/x_{\mathrm{FSWT}}$ in Fig. 6. In addition to data from Ref. [29] which corresponds to our samples, for which x_{NQR} is known, we include several other studies from the literature [49–54]. Since the latter do not include NQR data, we use the reported phase transition temperatures to extract x_{NQR} from our reconstructed phase diagram, as shown in Appendix A. The agreement between all studies in Fig. 6 is good, which validates our determination of the doping. The evolution of ϵ with x_{NQR} is compatible with a linear decrease which extrapolates to $\epsilon = 0$ for $x_{\mathrm{NQR}}/x_{\mathrm{FSWT}} = 0.96(6)$, i.e., when the low-frequency spectral weight vanishes. This is clear evidence of the low-doping-like regions fully accounting for the orthorhombicity of the material, and thus for the closely associated static magnetism.

B. Doping dependence

From Figs. 6 and 9, where all the samples considered in this paper are present, it can be seen that $x_{\mathrm{NQR}}/x_{\mathrm{FSWT}} = 0.40(4)$ (Oka-0.03; see Table I) is the highest doping for which a structural or magnetic transition is reported in a La-based sample, and $x_{\mathrm{NQR}}/x_{\mathrm{FSWT}} = 0.37(4)$ (one of our samples) the lowest one for which no such transition is observed. This defines a narrow threshold $x_{\mathrm{NQR}}/x_{\mathrm{FSWT}} \approx 0.39(3)$ beyond which only superconductivity occurs. For Ce samples this threshold is about 0.66(6) (Zhao-0.1, for which vanishing orthorhombicity is reported). For Sm samples it is at 0.67(2), i.e., between 0.75(10) (Martinelli-0.2) and 0.65(4) (one of our samples). Such values agree well with the known percolation thresholds for the nearest-neighbor square-lattice site problem in two and three dimensions, which given as dilution thresholds (i.e., the fraction of sites to remove) are respectively close to 0.41 and 0.69 [55–57]. This strongly suggests that the disappearance of orthorhombicity and static magnetism on doping is ultimately limited by the dilution of low-doping-like iron regions, without influence of the superconductivity.

The change from two-dimensionality (La) to three-dimensionality (Ce, Sm) indicates an enhanced coupling between the iron planes when the rare earth is Ce or Sm. Structural effects can be ruled out since there are only marginal differences, especially between La- and Ce-based compounds [58]. A more likely explanation is the magnetism of the rare earth (Ce, Sm) itself, whose $4f$ magnetic moment should increase interplane coupling compared to the nonmagnetic rare earth (La). Indeed, magnetic rare earths are known to couple to the $3d$ electrons [44,59–62], and are sufficiently coupled to each other to develop an ordered magnetic state at a few K. Note also that they should not significantly alter the in-plane couplings, as they lie directly above/below iron atoms. Such a situation is compatible with the parent compound having similar T_N for all rare earths. Indeed, for the small ratio $r = J_c/J_{ab}$ of the interplane to the intraplane coupling in 1111 compounds [63,64], T_N is predicted to vary little with r. As an example, assuming localized spins $S = 1/2$, a tripling of r from 0.001 to 0.003 yields only an increase of T_N by 13% [65]. In this picture of increased interplane coupling, it is interesting to note that the short-range-ordered (SRO) magnetism transition line of Ce and Sm samples shows a change in curvature between the dopings 0.34(2) and 0.50(2), i.e., about the 2D percolation threshold (see Fig. 4). On crossing the threshold, the in-plane density of low-doping-like regions becomes low enough that in-plane couplings between these regions are weakened, effectively increasing the dimensionality.

The observation of nearest-neighbor percolation thresholds may seem at odds with reports of 2D NN + NNN (nearest-neighbor + next-nearest-neighbor) percolation in La/Sm/Pr-1111 with ruthenium substitutions at iron sites [66–68]. There, spin dilution would cause static magnetism to vanish for $x_{\mathrm{Ru}} \approx 0.6$, close to the theoretical value 0.593 [69]. At first sight, such reports appear supported by the 1111 structure: it is expected that in-plane magnetic couplings occur between NN and NNN iron sites, i.e., that the J_1-J_2 model applies. However, there is significant evidence of a nonrandom distribution of Ru and microscopic phase separation in Ru-poor and Ru-rich regions [67,70–74], suggesting that the global Ru content is not the relevant parameter to describe percolation. In Appendix B, we propose a simple model to reinterpret the Sm-1111 NQR data of Sanna *et al.* [67] by assuming a phase separation in Fe-rich and Ru-rich regions. For the $x_{\mathrm{Ru}}^{\mathrm{nominal}} = 56\%$ composition, close to which static magnetism and superconductivity vanish, we find a volume fraction $\approx$48%

of Ru-rich regions with 80% local Ru concentration, which is likely too high to allow for any static magnetism of the iron atoms embedded in the nonmagnetic Ru matrix [75]. Static iron magnetism should instead originate from the ≈52% volume fraction of Fe-rich regions, which harbor low-doping-like (LD-like) areas as defined in the present paper. Due to the phase separation, the Ru-rich regions should be inefficient at preventing percolation of these LD-like areas. It is thus striking that the fraction of LD-like areas in the Fe-rich regions is equal to 0.274(66), i.e., consistent with 3D NN percolation (threshold equal to 0.31) rather than with 2D NN+NNN percolation (0.407). Although further study of the role of Ru substitutions is needed, this suggests agreement with the behavior observed by us in F-doped samples with a magnetic rare earth. Note that comparison with LaFeRuAsO using the NQR data of Ref. [76] could not be performed, since the very broad magnetic transitions for La-based samples [66–68] imply a more complicated distribution of ruthenium in the iron planes, for instance a variability of the ruthenium content in the iron-rich regions of each sample. Regarding the absence of NN+NNN percolation, it should be stressed that such percolation is expected in the context of a percolation site being equal to a single iron spin, i.e., by considering the J_1-J_2 model in electronically homogeneous iron layers. In the context of nanoscale separation into LD-like and HD-like regions, the elementary regions which percolate to yield static magnetism are likely larger than one lattice cell. Our result then suggests that these elementary regions interact through an effective NN interaction, whether local in character or involving the conduction electrons.

C. Mechanism

An immediate consequence of the observed percolation behavior is that the loss of static magnetism when doping is not related to a degradation of the nesting properties of the Fermi surface. An even more fundamental question about iron pnictides is whether the tightly related structural and magnetic transitions are driven by orbital or spin fluctuations [13]. In the presence of a magnetic rare earth, not only is 3D magnetism obtained on doping beyond the 2D percolation threshold, but orthorhombicity also occurs until the 3D percolation threshold (seemingly with an increased dimensionality [29]). Considering the crystal structure where R-(O,F)-R (R: rare earth) layers separate the FeAs layers, it is hard to explain how the unpaired $4f$ electrons of the rare earth would promote orbital correlations, rather than spin correlations. This suggests that the electronic anisotropy of the 1111 system at low doping is primarily driven by spin fluctuations, eventually yielding the enhanced, slow spin-nematic fluctuations seen below the structural transition [77,78], or at least that there is a decisive feedback of spin fluctuations on orbital fluctuations.

V. SUPERCONDUCTIVITY

The high-frequency, high-doping-like regions are natural candidates to harbor superconductivity. However, the superconducting volume fraction of 1111 materials appears to be large even at low doping [26]. Previous spin-lattice relaxation measurements also showed that the low- and high-frequency regions show a similar decrease of spin excitations

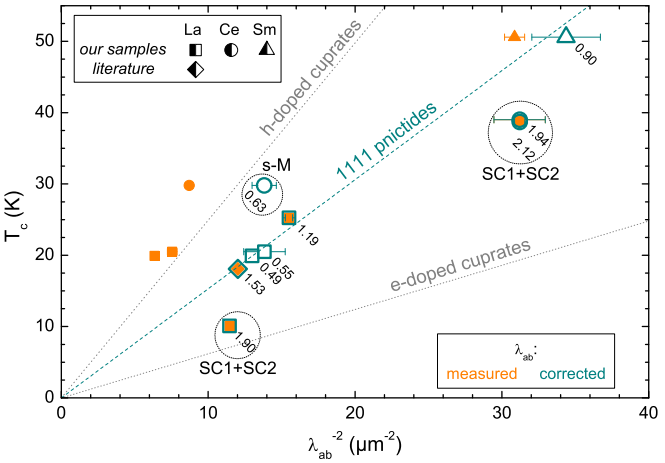

FIG. 7. Uemura plot showing the critical temperature vs λ_{ab}^{-2}. All measured data are taken from Refs. [22,29,80] (including one sample whose $x_{\mathrm{NQR}}/x_{\mathrm{FSWT}}$ is determined from its T_c value; see Appendix A). $x_{\mathrm{NQR}}/x_{\mathrm{FSWT}}$ is shown as a label. The uncertainty on λ_{ab}^{-2} is given for all samples where uncertainties on λ_{ab} and x_{NQR} are both available. The dashed line is a visual guide. Dotted lines indicate the behavior observed for hole-doped and electron-doped cuprates below or at optimal doping [81,82]. "s-M" refers to the presence of strong static magnetism, and "SC1+SC2" to the crossover between two superconducting states.

below T_c [21,33]. These observations could suggest that the low-frequency, low-doping-like regions support superconductivity when static magnetism is repressed, which is a crucial point with respect to ground-state competition and coexistence.

In La-1111, there is a significant decrease of the superfluid density ρ_s below optimal doping [22]. In the case where both ground states would coexist, competition for carriers would be expected. Such is the case in the 122 compound $Ba(Fe_{1-x}Co_x)_2As_2$, where a large enhancement of the penetration depth λ_{ab} is observed when the doping is low enough for coexistence [79]. λ_{ab}^2 is inversely proportional to ρ_s, whose decrease is argued to be due to the SDW partially gapping the Fermi surface, i.e., removing carriers. Even though no static magnetism is present in superconducting La-1111, it cannot be ruled out that the remaining slow spin fluctuations seen by NMR below optimal doping [30] are related to a partial gapping of the Fermi surface over some volume fraction of the samples. However, the observed decrease of ρ_s is much faster than that of T_c, yielding a Uemura plot (closed orange symbols in Fig. 7) where the pnictides show no well-defined slope as opposed to underdoped cuprates [82]. Taken at face value, this would suggest that superconductivity presents large variations of the coupling strength versus doping. Writing $\rho_s = n_s/m^*$ with n_s the superfluid carrier density and m^* the effective mass of the Cooper pairs, and considering the complex multiband structure, an explanation would be that changes in m^* occur with doping [20].

Here, we argue that the measured superfluid density (usually using μSR) is reduced for $x_{\mathrm{NQR}}/x_{\mathrm{FSWT}} < 1$ due to the proximity effect. Indeed, if only the HD-like regions are intrinsically superconducting, then their nanoscale coexistence with the LD-like regions implies that the proximity effect may

play over a large volume fraction, up to the entirety of the LD-like regions. Assuming the extremal case, the measured superfluid density then corresponds to a 100% SC volume fraction originating only from the HD-like regions, i.e.,

$$\rho_s^m = \rho_s^i \frac{x_{\mathrm{NQR}}}{x_{\mathrm{FSWT}}}, \tag{4}$$

where $\rho_s^{m/i}$ are the measured and intrinsic superfluid densities. Applying this correction to our samples for which penetration depth data is available [22,29,80], this yields a well-defined $T_c = f(n_s/m^*)$ slope, in-between that of hole- and electron-doped cuprates, for the La samples with $0.49 \leqslant x_{\mathrm{NQR}}/x_{\mathrm{FSWT}} \leqslant 1.53$ and for the Sm sample with $x_{\mathrm{NQR}}/x_{\mathrm{FSWT}} = 0.90$ (open turquoise symbols and visual guide in Fig. 7). This single slope indicates a common, well-defined superconducting state behavior, suggesting the validity of this scenario where only the HD-like regions intrinsically support superconductivity. Even in the absence of static magnetism, the LD-like regions do not appear to contribute to the condensate. This suggests that in the undoped limit there is no underlying superconducting ground state which static magnetism would be suppressing. The implications for the mechanism responsible for Cooper pairing are also strong, since the linearity of T_c on ρ_s would seem to rule out theoretical approaches in the weak-coupling limit [83].

Note that, for dopings where the material is electronically inhomogeneous ($x_{\mathrm{NQR}}/x_{\mathrm{FSWT}} < 1$), it cannot be said that the observed behavior is that of a material that is simply less doped than x_{FSWT}. The observed Uemura relation then rather reflects the properties of x_{FSWT}-like superconductivity which is weakened due to the interspersed low-doping-like and high-doping-like regions. This seems however to be equivalent to a doping variation, since the electronically homogeneous, roughly optimally doped $x_{\mathrm{NQR}}/x_{\mathrm{FSWT}} = 1.19$ La-based sample obeys the same behavior. For La samples with even higher $x_{\mathrm{NQR}}/x_{\mathrm{FSWT}}$, whose T_c would suggest they are overdoped, the Uemura relation appears to be maintained through the concomitant decrease of T_c and ρ_s up to at least $x_{\mathrm{NQR}}/x_{\mathrm{FSWT}} = 1.53$, and breaks for $x_{\mathrm{NQR}}/x_{\mathrm{FSWT}} = 1.90$ which shows a reduced T_c and a still moderate superfluid density. This is unlike the behavior observed in cuprates, where overdoping tends to result in a saturation then a decrease of T_c as ρ_s keeps increasing [82]. Here, the $x_{\mathrm{NQR}}/x_{\mathrm{FSWT}} = 1.53$ La-based sample is behaving like an underdoped sample, suggesting that the observed T_c dome is misleading. Note that this is in agreement with the study of hydrogen-doped 1111 pnictides by Iimura *et al.* [45], who report that the decrease of T_c beyond optimal doping may be due to a degradation of the nesting of the Fermi surface and of the associated spin fluctuations. Concerning the $x_{\mathrm{NQR}}/x_{\mathrm{FSWT}} = 1.90$ La-based sample, it is interesting to note that the breakdown of the Uemura relation occurs in the region of the phase diagram where T_c is depressed (see Fig. 4), which corresponds to a crossover between two different superconducting states (SC1 and SC2) [45]. Assuming that SC1 and SC2 may be competing but do not support each other, we define in the following $T_c^{(1),(2)}$ as their respective critical temperatures at a given doping, and $\rho_s^{(1),(2)}$ as their respective contributions to the total superfluid density ρ_s. For $x_{\mathrm{NQR}}/x_{\mathrm{FSWT}} = 1.90$, Fig. 4 indicates $T_c^{(1)} > T_c^{(2)}$. While the available data are insufficient to conclude, a possible scenario is then that the Uemura relation is still obeyed for SC1 with $T_c = T_c^{(1)}$, and with $\rho_s^{(2)}$ accounting for the apparent breakdown. For highly doped Ce-based samples, the breakdown of the Uemura relation could have a similar explanation. Finally, the insufficient correction of the superfluid density observed for the $x_{\mathrm{NQR}}/x_{\mathrm{FSWT}} = 0.63$ Ce-based sample will be linked to ground-state competition in Sec. VI.

Our result on the presence of a full-volume proximity effect allows us to put an upper boundary ξ_N on the typical distance d_{H-H} separating HD-like regions, with ξ_N the coherence length in the normal material, i.e., the characteristic length over which the pair amplitude decays. For similarly poor conductors such as cuprates, ξ_N can be expected to be on the order of a few nanometers. Since the LD-like regions are unable to support superconductivity by themselves, it is possible to rule out an enhancement of ξ_N at low temperature such as that observed in Josephson junctions where two superconducting, high-T_c cuprate electrodes are separated by an underdoped, lower-T_c cuprate barrier in the normal state [84,85]. The small value of d_{H-H}, together with the conducting electronic background, favors the strong coupling of the intrinsically superconducting regions [86]. This may explain why, in the absence of static magnetism, a sample with $x_{\mathrm{NQR}}/x_{\mathrm{FSWT}}$ as low as 0.49 (La-based sample) still achieves a T_c as high as ≈75% of the optimal value. Such a strong coupling was also proposed to explain the resilience of superconductivity in Ru-doped Ba-122 [19]. Finally, the high-doping-like regions should be at least of size ξ_S, the superconducting coherence length. This translates to about 20–40 Å in the *ab* plane [87,88]. Therefore, a patchwork of regions a few nanometers across is the most simple arrangement compatible with the observed superconducting behavior. A similar conclusion was reached by Sanna *et al.* on the basis of the magnetic behavior [4,32].

VI. INTERPLAY OF THE GROUND STATES

In light of the detrimental effect of iron static magnetism on superconductivity (see Sec. III D), ground-state coexistence appears as a special case where static magnetism from the LD-like regions may restrict the spatial extension of superconductivity originating from the HD-like regions. Indeed, such a behavior seems present in the $x_{\mathrm{NQR}}/x_{\mathrm{FSWT}} = 0.63$ Ce-based sample. As seen in Fig. 7, correcting the superfluid density of this sample according to Eq. (4) is not enough to bring it in agreement with the observed Uemura relation. This suggests a loss of superfluid density, on contrary to the samples without ground-state coexistence. According to μSR the magnetic volume fraction reaches 100%, with a freezing of the iron moments over an extended temperature range (≈5–26 K) [29]. Such a distribution of T_N is a common feature [4,6,7,32]. The 100% volume fraction does not mean that the whole sample is intrinsically magnetic, which would be incompatible with our results, but that the field from the magnetically ordered LD-like regions is also felt in the HD-like regions due to the nanoscale separation. At a given T_N, the corresponding magnetic regions and their nanometer-scale environment will show up as frozen volume in the μSR measurement. In isovalently doped $Ba(Fe_{1-x}Ru_x)_2As_2$, the distribution of T_N was ascribed to a spatial variation of the ordered iron moment,

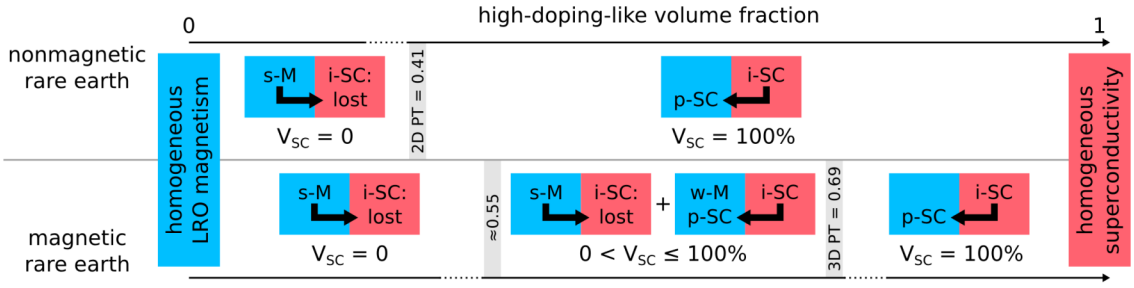

FIG. 8. Summary of the interplay of ground states in the doping range where LD-like (blue) and HD-like (red) regions coexist at the nanoscale. The LD-like regions can feature strong ("s-M") or weak ("w-M") static magnetism, as well as superconductivity through proximity ("p-SC"). The HD-like regions feature intrinsic superconductivity ("i-SC"), which can be suppressed ("i-SC: lost"). V_{SC} is the superconducting volume fraction, while "LRO" and "PT" stand for "long-range ordered" and "percolation threshold." For the magnetic rare-earth case, the intermediate doping region ($0 < V_{SC} \leqslant 100\%$) is simplified by not making a distinction between strong static magnetism preventing superconductivity by proximity and destroying nearby intrinsic superconductivity, and by not detailing the behavior close to the 3D percolation threshold, where all of the static magnetism is expected to be weak enough for $V_{SC} \approx 100\%$.

with values smaller than about $0.3\mu_B$ allowing for local coexistence of superconductivity and static magnetism [19]. In F-doped 1111 pnictides, the variation of the strength of static magnetism could be due to finite-size effects and to the disorder inherent to a transition with percolative character (see Sec. IV). The LD-like regions with the strongest magnetism (highest T_N) will locally suppress superconductivity by proximity, and possibly also the intrinsic superconductivity in the nearest HD-like regions, whereas the LD-like regions with weak or zero static magnetism will tolerate it. In such a picture some superfluid density is irremediably lost in or close to the more magnetic regions, in agreement with the observed breakdown of the Uemura relation. This would also explain the report of a reduced superconducting volume fraction in the presence of ground-state coexistence [4].

All our results which pertain to the existence and the interplay of static magnetism and superconductivity are summarized in Fig. 8. In the parent compound, the paramagnetic state is electronically homogeneous, yielding the well-known long-range-ordered magnetic phase at low temperature. On increasing the doping, nonmagnetic HD-like regions start to appear, while T_N decreases. The static magnetism from the LD-like regions is nonetheless still strong enough to suppress any superconductivity that may have emerged from the HD-like regions, thus a zero superconducting volume fraction (V_{SC}). For the nonmagnetic rare earth (La), orthorhombicity and static magnetism cannot occur beyond the 2D nearest-neighbor percolation threshold. The development of superconductivity is then no longer hampered anywhere in the material, and V_{SC} jumps to 100% due to superconductivity by proximity in the LD-like regions. A homogeneous, purely intrinsic superconducting state is eventually reached when the LD-like regions have disappeared. For the magnetic rare earths (Ce, Sm) static magnetism survives to higher doping, allowing for a distribution of T_N that crosses progressively into a low-temperature range: the LD-like regions with weaker magnetism are no longer able to suppress superconductivity originating from the nearby HD-like regions, and V_{SC} starts to grow. This occurs at $x_{NQR}/x_{FSWT} \approx 0.55$, i.e., in-between 0.50 (purely magnetic Ce sample) and 0.59 (magnetic and superconducting Sm sample), with the approximation that the boundary is the same for Ce- and Sm-based compounds. On approaching the 3D nearest-neighbor percolation threshold ($x_{NQR}/x_{FSWT} \approx 0.69$), T_N should be systematically low before actually vanishing. Intrinsic superconductivity in the HD-like regions is then never suppressed, nor is superconductivity by proximity in the LD-like regions. Again, a homogeneous superconducting state is reached for $x_{NQR} = x_{FSWT}$. While this scenario accounts well for the qualitative difference between the phase diagrams of nonmagnetic and magnetic rare earths [3,4,22,32], note that a small coexistence region cannot be ruled out for La-based samples, as suggested by measurements on hydrogen-doped samples [89]. Any such coexistence region will be limited to the very narrow doping range ($x_{NQR}/x_{FSWT} = 0.39 \pm 0.03$; see Sec. IV) over which static magnetism could be weakened enough to allow for the presence of superconductivity. It should also be noted that for Ce- and Sm-based samples at intermediate doping, the detailed evolution of V_{SC} should depend not only on the distribution in the strength of the static magnetism but also on the microscopic arrangement of LD-like and HD-like regions, which will affect how much superconductivity is suppressed.

VII. CONCLUSION

The phase diagram of 1111 $R\mathrm{FeAsO}_{1-x}\mathrm{F}_x$ (R = La, Ce, Sm) iron pnictides has been constructed as a function of the NQR spectral properties in the paramagnetic state, i.e., the properties of two types of local charge distributions associated to low-doping-like (LD-like) and high-doping-like (HD-like) regions. The combination of a local probe technique and relative intensity measurements results in high accuracy and consistency across all measured samples. This allows us to show without any ambiguity that magnetic rare earths (Ce, Sm) promote iron static magnetism to higher doping, with a detrimental effect on superconductivity. Besides, our approach allows for successful inclusion of NQR data from other groups with different sample sources, yielding to our knowledge the most extensive phase diagram for fluorine-doped La-based compounds, including the upturn of the superconducting transition temperature at high doping.

Using the NQR-defined doping, as directly measured for our samples or as derived from our phase diagram for studies using other techniques, we have investigated the spatial origin

of static magnetism and superconductivity. It is found that the LD-like regions are closely associated to the development of orthorhombicity and static magnetism, with the upper doping limit set by dilution effects: 2D (respectively 3D) nearest-neighbor square lattice site percolation is at play when the rare earth is nonmagnetic (respectively magnetic). The LD-like regions are not intrinsically supportive of superconductivity but can harbor superconductivity by proximity, originating from the nearby HD-like regions, whenever static magnetism is weak enough. In the end, the interplay of ground states in 1111 pnictides appears to be well described as a spatial competition between nanoscopic regions, which compete to establish the ground state through suppression of superconductivity by static magnetism, and extension of superconductivity by proximity effect.

Our conclusions are compatible with various observations taken from the literature, whether associated to static magnetism, such as a pseudogaplike feature that survives up to $T \approx 140$ K in superconducting samples and the Nernst signature of a possible SDW precursor in an underdoped superconducting sample without static magnetism [90,91], or associated to superconductivity, such as the presence of additional pinning due to nanoscale regions with suppressed superconductivity and the possibly related enhancement of the upper critical field H_{c2} and $dH_{c2}/dT(T_c)$ at low doping [92,93]. The well-defined Uemura relation is also in agreement with work supporting the strong-coupling nature of superconductivity in iron pnictides [94]. Besides, our scenario eliminates the controversy surrounding the "first-order-like" transition in the $R =$ La phase diagram from magnetically ordered samples to superconducting samples. Rather than a smooth evolution of the ground state throughout the whole sample volume, the conditions for magnetic order or superconductivity are already met on a local scale, with the switching of the ground state being dependent on percolation.

Through a better understanding of ground-state competition and of the nature of superconductivity, our results should help bring insight on the origin of unconventional superconductivity in iron pnictides. Further work should address the origin and the details of the nanoscopic arrangement of magnetism-prone and superconductivity-prone regions, for which some theory leads exist [95,96], as well as the applicability of our picture of ground-state interplay to other iron pnictide families. The latter appear to feature similar physics of the FeAs layers, but in a more homogeneous context. It would also be of interest to better understand the local charge arrangement giving rise to the observed EFG, in the doping range studied here but also with respect to its reported evolution at very high doping [97,98].

ACKNOWLEDGMENTS

We acknowledge insightful discussions with N. Bergeal, B. Büchner, S. Caprara, L. de' Medici, A. Descamps-Mandine, B. Fauqué, C. Feuillet-Palma, J. E. Hamann-Borrero, J. Jeanneau, A. Trokiner, as well as experimental support from R. Müller, K. Leger, C. Malbrich, and M. Deutschmann (synthesis), S. Müller-Litvanyi and G. Kreutzer (SEM-WDX), C. G. F. Blum (XRD), O. Vakaliuk (resistivity), S. Gaß and R. Vogel (NQR). This work was supported by the Deutsche Forschungsgemeinschaft (DFG) through FOR 538, SPP 1458 (Grants No. BE1749/13 and No. GR3330/2), and the Emmy Noether programme (Grant No. WU595/3-1).

APPENDIX A: DOPING DETERMINATIONS USING THE RECONSTRUCTED PHASE DIAGRAM

Using the phase diagram obtained in Sec. III, it is possible to extract $x_{\mathrm{NQR}}/x_{\mathrm{FSWT}}$ for samples from the literature whose phase-transition temperatures are known, without the need for NQR data. As shown in Fig. 9, this has been done for a number of samples (listed in Table II) whose properties (orthorhombicity, penetration depth) are of interest for Secs. IV and V. Agreement could be achieved for samples showing more than one transition, with the exception of the samples from Ref. [54]. The latter feature structural phase-transition temperatures which are unusually high, due to a specific analysis of synchrotron data which is sensitive to incipient order. For these samples, priority in setting x_{NQR} is then given to the magnetic and superconducting phase transitions.

APPENDIX B: PHASE SEPARATION IN Ru-SUBSTITUTED COMPOUNDS

Following the observation of microscopic phase separation in Fe-rich and Ru-rich regions in 1111 samples where iron has been partially substituted with ruthenium [67,70–74], we propose a simple model to reinterpret the data of Ref. [67]. Applying NQR to $SmFe_{1-x}Ru_xAsO_{0.85}F_{0.15}$, Sanna *et al.* obtain spectra featuring low- and high-frequency components like ours but also four more peaks corresponding to As nuclei with 1/2/3/4 Ru nearest neighbors (NNs). We write the corresponding experimental spectral weights as w_p^{exp} with $p =$ L/H/1/2/3/4. For the $x_{\mathrm{Ru}}^{\mathrm{nominal}} = 0.56$ compound, in which static magnetism and superconductivity are on the verge of vanishing, NQR yields the weights given in Table III (as well as $w_H^{\mathrm{exp}} = 0$). As then noted there is a tendency towards Ru

TABLE II. Samples from the literature which are included in Figs. 6 and 7. x indicates the fluorine doping as given in the source paper, which is usually the nominal value. $x_{\mathrm{NQR}}/x_{\mathrm{FSWT}}$ is derived from Fig. 9.

Rare earth	Source - first author	x	$x_{\mathrm{NQR}}/x_{\mathrm{FSWT}}$
La	[22] - Luetkens	0.125	1.53(6)
	[49] - Huang	0.03	0.15(7)
		0.05	0.36(4)
	[50] - Qureshi	0.045	0.22(6)
Ce	[51] - Zhao	0.02	0.10(7)
		0.04	0.28(5)
		0.06	0.51(4)
		0.08	0.59(3)
		0.1	0.66(6)
Sm	[54] - Martinelli	0.05	0.30(5)
		0.075	0.35(5)
		0.1	0.64(6)
		0.2	0.75(10)
	[52] - Margadonna	0.05	0.40(8)
		0.1	0.52(4)
		0.12	0.55(4)

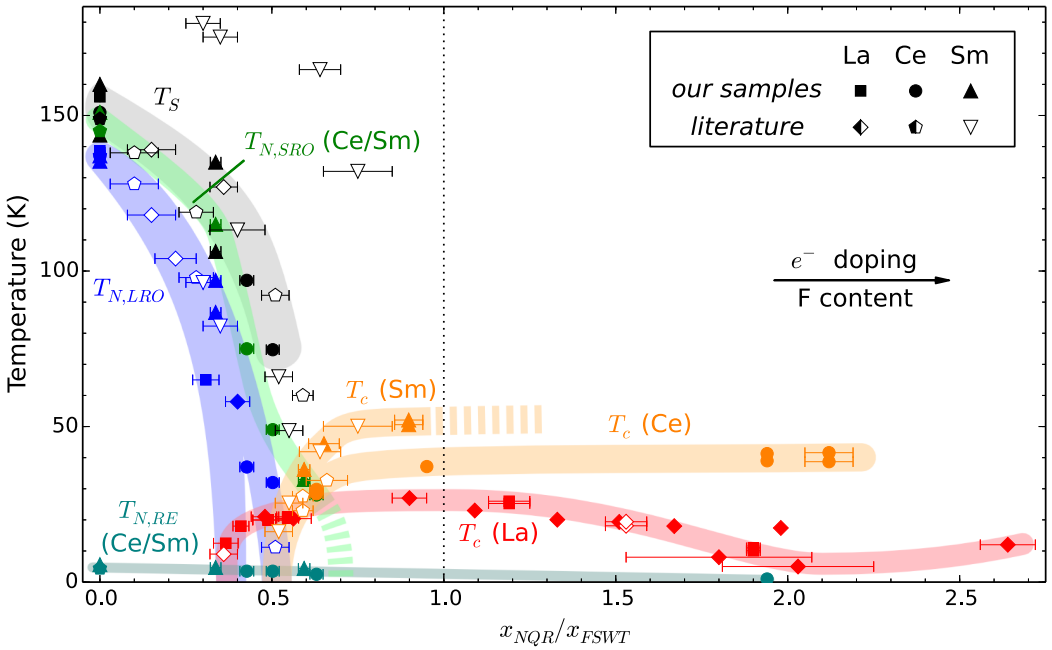

FIG. 9. Phase diagram as used for the determination of $x_{\mathrm{NQR}}/x_{\mathrm{FSWT}}$ for samples from the literature, whose phase-transition temperatures are known but for which no NQR data are available (open symbols). These samples are listed in Table II. The closed symbols correspond to the samples used to determine the phase diagram (see also Fig. 4).

clustering, with w_4^{exp} being twice larger than expected for a binomial distribution (see w_p^{bin} in Table III).

Beyond phase separation into Fe-rich and Ru-rich regions, our model is built on these hypotheses: (i) each type of region features binomial statistics corresponding to the local Ru concentration; (ii) the phase separation is sufficiently marked that the Fe-rich regions harbor almost all As with zero or one Ru NN, and the Ru-rich regions almost all As with four Ru NNs. In the following, all quantities related to the Fe- and Ru-rich regions are respectively indicated by the exponents "i" and "r."

We first derive all compositional quantities. The Ru content in the Fe-rich regions x_{Ru}^i is given by:

$$\frac{\left(1-x_{\mathrm{Ru}}^i\right)^4}{4x_{\mathrm{Ru}}^i\left(1-x_{\mathrm{Ru}}^i\right)^3} \overset{\text{(i)}}{=} \frac{w_L^i}{w_1^i} \overset{\text{(ii)}}{\approx} \frac{w_L^{\mathrm{exp}}}{w_1^{\mathrm{exp}}},$$

TABLE III. Spectral weights for the local environments seen by NQR in $SmFe_{0.44}Ru_{0.56}AsO_{0.85}F_{0.15}$ (see text). The experimental data are taken from Ref. [67], and the experimental uncertainty is assumed to be the point size of the original figure.

	Experiment	Binomial	Model		
p	w_p^{exp}	w_p^{bin}	w_p^i	w_p^r	w_p^{calc}
L	0.142(26)	0.037	0.274(66)	0.001(1)	0.143(26)
1	0.217(26)	0.191	0.419(10)	0.024(13)	0.229(20)
2	0.251(26)	0.364	0.240(47)	0.149(45)	0.196(24)
3	0.189(26)	0.309	0.061(25)	0.408(22)	0.228(26)
4	0.201(26)	0.098	0.006(4)	0.417(81)	0.204(26)

where the two equalities derive from hypotheses (i) and (ii). This yields $x_{Ru}^i = 0.276(44)$, thus the w_p^i weights in Table III. The volume fraction of Fe-rich regions is given by:

$$V^i \overset{\text{(ii)}}{\approx} \frac{w_L^{\mathrm{exp}}}{w_L^i} = 0.518(69).$$

The Ru content in the Ru-rich regions x_{Ru}^r is given by

$$\left(x_{\mathrm{Ru}}^r\right)^4 \overset{\text{(i)}}{=} w_4^r \overset{\text{(ii)}}{\approx} \frac{w_4^{\mathrm{exp}}}{(1-V^i)},$$

yielding $x_{\mathrm{Ru}}^r = 0.804(39)$, thus the w_p^r weights in Table III. The calculated Ru content of the whole sample is given by

$$x_{\mathrm{Ru}}^{\mathrm{calc}} = V^i x_{\mathrm{Ru}}^i + (1-V^i)x_{\mathrm{Ru}}^r = 0.531(22).$$

The spectral weights for the whole sample are given by

$$w_p^{\mathrm{calc}} = V^i w_p^i + (1-V^i)w_p^r,$$

with $p = L/1/2/3/4$, yielding the w_p^{calc} weights in Table III.

We then check the consistency of the calculation. The consistency of hypothesis (ii) is shown by the following population ratios being small:

$$\frac{w_L^r(1-V^i)}{w_L^i V^i} = 0.005(5),$$
$$\frac{w_1^r(1-V^i)}{w_1^i V^i} = 0.054(41),$$
$$\frac{w_4^i V^i}{w_4^r(1-V^i)} = 0.015(11).$$

This is also reflected in $w_p^{\mathrm{calc}} \approx w_p^{\mathrm{exp}}$ for $p = L/1/4$, and reasonable agreement is found for $p = 2/3$. The small differences should be attributed to the phase boundaries and to minor deviations from randomness inside the Fe-rich and Ru-rich regions. Finally, the slightly reduced value of $x_{\mathrm{Ru}}^{\mathrm{calc}}$ compared to $x_{\mathrm{Ru}}^{\mathrm{nominal}}$ is in agreement with experimental determinations [76,99]. Therefore, our simple model appears to be in good quantitative agreement with the experiment. It is likely complementary to that of Ref. [74], which cannot easily distinguish the quantitative properties of the iron-rich and ruthenium-rich regions, but provides microscopic arrangements compatible with NQR measurements.

[1] G. R. Stewart, Superconductivity in iron compounds, Rev. Mod. Phys. **83**, 1589 (2011).

[2] C. Wang, S. Jiang, Q. Tao, Z. Ren, Y. Li, L. Li, C. Feng, J. Dai, G. Cao, and Z.-a. Xu, Superconductivity in $LaFeAs_{1-x}P_x$ O: Effect of chemical pressures and bond covalency, Europhys. Lett. **86**, 47002 (2009).

[3] A. J. Drew, Ch. Niedermayer, P. J. Baker, F. L. Pratt, S. J. Blundell, T. Lancaster, R. H. Liu, G. Wu, X. H. Chen, I. Watanabe, V. K. Malik, A. Dubroka, M. Rössle, K. W. Kim, C. Baines, and C. Bernhard, Coexistence of static magnetism and superconductivity in $SmFeAsO_{1-x}F_x$ as revealed by muon spin rotation, Nat. Mater. **8**, 310 (2009).

[4] S. Sanna, R. De Renzi, G. Lamura, C. Ferdeghini, A. Palenzona, M. Putti, M. Tropeano, and T. Shiroka, Magnetic-superconducting phase boundary of $SmFeAsO_{1-x}F_x$ studied via muon spin rotation: Unified behavior in a pnictide family, Phys. Rev. B **80**, 052503 (2009).

[5] J. P. Carlo, Y. J. Uemura, T. Goko, G. J. MacDougall, J. A. Rodriguez, W. Yu, G. M. Luke, P. Dai, N. Shannon, S. Miyasaka, S. Suzuki, S. Tajima, G. F. Chen, W. Z. Hu, J. L. Luo, and N. L. Wang, Static Magnetic Order and Superfluid Density of R FeAs(O, F) (R = La, Nd, Ce) and LaFePO Studied by Muon Spin Relaxation: Unusual Similarities with the Behavior of Cuprate Superconductors, Phys. Rev. Lett. **102**, 087001 (2009).

[6] T. Shiroka, G. Lamura, S. Sanna, G. Prando, R. De Renzi, M. Tropeano, M. R. Cimberle, A. Martinelli, C. Bernini, A. Palenzona, R. Fittipaldi, A. Vecchione, P. Carretta, A. S. Siri, C. Ferdeghini, and M. Putti, Long- to short-range magnetic order in fluorine-doped CeFeAsO, Phys. Rev. B **84**, 195123 (2011).

[7] G. Lamura, T. Shiroka, P. Bonfà, S. Sanna, R. De Renzi, M. Putti, N. D. Zhigadlo, S. Katrych, R. Khasanov, and J. Karpinski, Slow magnetic fluctuations and superconductivity in fluorine-doped NdFeAsO, Phys. Rev. B **91**, 024513 (2015).

[8] Y. Laplace, J. Bobroff, F. Rullier-Albenque, D. Colson, and A. Forget, Atomic coexistence of superconductivity and incommensurate magnetic order in the pnictide $Ba(Fe_{1-x}Co_x)_2As_2$, Phys. Rev. B **80**, 140501(R) (2009).

[9] M.-H. Julien, H. Mayaffre, M. Horvatić, C. Berthier, X. D. Zhang, W. Wu, G. F. Chen, N. L. Wang, and J. L. Luo, Homogeneous vs. inhomogeneous coexistence of magnetic order and superconductivity probed by NMR in Co- and K-doped iron pnictides, Europhys. Lett. **87**, 37001 (2009).

[10] E. Wiesenmayer, H. Luetkens, G. Pascua, R. Khasanov, A. Amato, H. Potts, B. Banusch, H.-H. Klauss, and D. Johrendt, Microscopic Coexistence of Superconductivity and Magnetism in $Ba_{1-x}K_xFe_2As_2$, Phys. Rev. Lett. **107**, 237001 (2011).

[11] M. M. Korshunov and I. Eremin, Theory of magnetic excitations in iron-based layered superconductors, Phys. Rev. B **78**, 140509(R) (2008).

[12] C. de la Cruz, Q. Huang, J. W. Lynn, J. Li, W. Ratcliff II, J. L. Zarestky, H. A. Mook, G. F. Chen, J. L. Luo, N. L. Wang, and P. Dai, Magnetic order close to superconductivity in the iron-based layered $LaO_{1-x}F_xFeAs$ systems, Nature (London) **453**, 899 (2008).

[13] R. M. Fernandes, A. V. Chubukov, and J. Schmalian, What drives nematic order in iron-based superconductors? Nat. Phys. **10**, 97 (2014).

[14] A. V. Chubukov, D. V. Efremov, and I. Eremin, Magnetism, superconductivity, and pairing symmetry in iron-based superconductors, Phys. Rev. B **78**, 134512 (2008).

[15] I. I. Mazin, D. J. Singh, M. D. Johannes, and M. H. Du, Unconventional Superconductivity with a Sign Reversal in the Order Parameter of $LaFeAsO_{1-x}F_x$, Phys. Rev. Lett. **101**, 057003 (2008).

[16] K. Kuroki, S. Onari, R. Arita, H. Usui, Y. Tanaka, H. Kontani, and H. Aoki, Unconventional Pairing Originating from the Disconnected Fermi Surfaces of Superconducting $LaFeAsO_{1-x}F_x$, Phys. Rev. Lett. **101**, 087004 (2008).

[17] H. Kontani and S. Onari, Orbital-Fluctuation-Mediated Superconductivity in Iron Pnictides: Analysis of the Five-Orbital Hubbard-Holstein Model, Phys. Rev. Lett. **104**, 157001 (2010).

[18] Y. Texier, Y. Laplace, P. Mendels, J. T. Park, G. Friemel, D. L. Sun, D. S. Inosov, C. T. Lin, and J. Bobroff, Mn local moments prevent superconductivity in iron pnictides $Ba(Fe_{1-x}Mn_x)_2As_2$, Europhys. Lett. **99**, 17002 (2012).

[19] Y. Laplace, J. Bobroff, V. Brouet, G. Collin, F. Rullier Albenque, D. Colson, and A. Forget, Nanoscale-textured superconductivity in Ru-substituted $BaFe_2As_2$: A challenge to a universal phase diagram for the pnictides, Phys. Rev. B **86**, 020510(R) (2012).

[20] F. Hammerath, P. Bonfà, S. Sanna, G. Prando, R. De Renzi, Y. Kobayashi, M. Sato, and P. Carretta, Poisoning effect of Mn in $LaFe_{1-x}Mn_xAsO_{0.89}F_{0.11}$: Unveiling a quantum critical point in the phase diagram of iron-based superconductors, Phys. Rev. B **89**, 134503 (2014).

[21] G. Lang, H.-J. Grafe, D. Paar, F. Hammerath, K. Manthey, G. Behr, J. Werner, and B. Büchner, Nanoscale Electronic Order in Iron Pnictides, Phys. Rev. Lett. **104**, 097001 (2010).

[22] H. Luetkens, H.-H. Klauss, M. Kraken, F. J. Litterst, T. Dellmann, R. Klingeler, C. Hess, R. Khasanov, A. Amato, C. Baines, M. Kosmala, O. J. Schumann, M. Braden, J. Hamann-Borrero, N. Leps, A. Kondrat, G. Behr, J. Werner, and B. Büchner, The electronic phase diagram of the $LaO_{1-x}F_xFeAs$ superconductor, Nat. Mater. **8**, 305 (2009).

[23] A. Köhler and G. Behr, WDX-analysis of the new superconductors $RO_{1-x}F_xFeAs$ and its consequences on the electronic phase diagram, J. Supercond. Nov. Magn. **22**, 565 (2009).

[24] C. R. Rotundu, D. T. Keane, B. Freelon, S. D. Wilson, A. Kim, P. N. Valdivia, E. Bourret-Courchesne, and R. J. Birgeneau,

Phase diagram of the $PrFeAsO_{1-x}F_x$ superconductor, Phys. Rev. B **80**, 144517 (2009).

[25] M. Fujioka, S. J. Denholme, T. Ozaki, H. Okazaki, K. Deguchi, S. Demura, H. Hara, T. Watanabe, H. Takeya, T. Yamaguchi, H. Kumakura, and Y. Takano, Phase diagram and superconductivity at 58.1 K in α-FeAs-free $SmFeAsO_{1-x}F_x$, Supercond. Sci. Technol. **26**, 085023 (2013).

[26] A. Kondrat, J. E. Hamann-Borrero, N. Leps, M. Kosmala, O. Schumann, A. Köhler, J. Werner, G. Behr, M. Braden, R. Klingeler, B. Büchner, and C. Hess, Synthesis and physical properties of $LaO_{1-x}F_xFeAs$, Eur. Phys. J. B **70**, 461 (2009).

[27] C. Hess, A. Kondrat, A. Narduzzo, J. E. Hamann-Borrero, R. Klingeler, J. Werner, G. Behr, and B. Büchner, The intrinsic electronic phase diagram of iron-oxypnictide superconductors, Europhys. Lett. **87**, 17005 (2009).

[28] R. Klingeler, N. Leps, I. Hellmann, A. Popa, U. Stockert, C. Hess, V. Kataev, H.-J. Grafe, F. Hammerath, G. Lang, S. Wurmehl, G. Behr, L. Harnagea, S. Singh, and B. Büchner, Local antiferromagnetic correlations in the iron pnictide superconductors $LaFeAsO_{1-x}F_x$ and $Ca(Fe_{1-x}Co_x)_2As_2$ as seen via normal-state susceptibility, Phys. Rev. B **81**, 024506 (2010).

[29] H. Maeter, J. E. Hamann-Borrero, T. Goltz, J. Spehling, A. Kwadrin, A. Kondrat, L. Veyrat, G. Lang, H.-J. Grafe, C. Hess, G. Behr, B. Büchner, H. Luetkens, C. Baines, A. Amato, N. Leps, R. Klingeler, R. Feyerherm, D. Argyriou, and H.-H. Klauss, Structural and electronic phase diagrams of $CeFeAsO_{1-x}F_x$ and $SmFeAsO_{1-x}F_x$, arXiv:1210.6959.

[30] F. Hammerath, U. Gräfe, T. Kühne, H. Kühne, P. L. Kuhns, A. P. Reyes, G. Lang, S. Wurmehl, B. Büchner, P. Carretta, and H.-J. Grafe, Progressive slowing down of spin fluctuations in underdoped $LaFeAsO_{1-x}F_x$, Phys. Rev. B **88**, 104503 (2013).

[31] A. Abragam, *The Principles of Nuclear Magnetism* (Oxford University Press, Oxford, 1961).

[32] S. Sanna, R. De Renzi, T. Shiroka, G. Lamura, G. Prando, P. Carretta, M. Putti, A. Martinelli, M. R. Cimberle, M. Tropeano, and A. Palenzona, Nanoscopic coexistence of magnetic and superconducting states within the FeAs layers of $CeFeAsO_{1-x}F_x$, Phys. Rev. B **82**, 060508(R) (2010).

[33] T. Oka, Z. Li, S. Kawasaki, G. F. Chen, N. L. Wang, and G.-q. Zheng, Antiferromagnetic Spin Fluctuations Above the Dome-Shaped and Full-Gap Superconducting States of $LaFeAsO_{1-x}F_x$ Revealed by ^{75}As-Nuclear Quadrupole Resonance, Phys. Rev. Lett. **108**, 047001 (2012).

[34] S. Kawasaki, T. Mabuchi, S. Maeda, T. Adachi, T. Mizukami, K. Kudo, M. Nohara, and G.-q. Zheng, Doping-enhanced antiferromagnetism in $Ca_{1-x}La_xFeAs_2$, Phys. Rev. B **92**, 180508(R) (2015).

[35] S. Kitagawa, Y. Nakai, T. Iye, K. Ishida, Y. Kamihara, M. Hirano, and H. Hosono, F-doping dependence of ^{75}As nuclear quadrupole resonance frequency in $LaFeAs(O_{1-x}F_x)$, Physica C **470**, S282 (2010).

[36] K. Tatsumi, N. Fujiwara, H. Okada, H. Takahashi, Y. Kamihara, M. Hirano, and H. Hosono, ^{75}As-NMR studies on $LaFeAsO_{1-x}F_x$ ($x = 0.14$) under a pressure of 3 GPa, J. Phys. Soc. Jpn. **78**, 023709 (2009).

[37] H. Mukuda, M. Nitta, M. Yashima, Y. Kitaoka, P. M. Shirage, H. Eisaki, and A. Iyo, Coherence effect of sign-reversing $s_{\pm}$-wave Cooper pair state in heavily overdoped LaFeAsO-based superconductor: ^{75}As-nuclear quadrupole resonance, J. Phys. Soc. Jpn. **79**, 113701 (2010).

[38] Y. Kobayashi, E. Satomi, S. C. Lee, and M. Sato, ^{75}As-NMR studies of $LaFeAsO_{1-x}F_x$ for various x values, J. Phys. Soc. Jpn. **79**, 093709 (2010).

[39] M. Nitta, H. Mukuda, M. Yashima, Y. Kitaoka, P. M. Shirage, H. Eisaki, and A. Iyo, ^{75}As-NQR and ^{57}Fe-NMR studies on heavily overdoped LaFeAsO-based superconductors, J. Phys. Soc. Jpn. **81**, SB044 (2012).

[40] Z.-A. Ren, W. Lu, J. Yang, W. Yi, X.-L. Shen, Z.-C. Li, G.-C. Che, X.-L. Dong, L.-L. Sun, F. Zhou, and Z.-X. Zhao, Superconductivity at 55 K in iron-based F-doped layered quaternary compound $Sm[O_{1-x}F_x]FeAs$, Chin. Phys. Lett. **25**, 2215 (2008).

[41] H. Yamashita, M. Yashima, H. Mukuda, Y. Kitaoka, P. M. Shirage, and A. Iyo, NMR study of Fe-oxypnictide superconductors RE-Fe-As-O (RE = Nd, Pr, $La_{0.7}Y_{0.3}$), Physica C **470**, S375 (2010).

[42] D. Rybicki, T. Meissner, G. V. M. Williams, S. V. Chong, M. Lux, and J. Haase, ^{75}As NMR study of overdoped $CeFeAsO_{0.8}F_{0.2}$, J. Phys.: Condens. Matter **25**, 315701 (2013).

[43] K. Ahilan, F. L. Ning, T. Imai, A. S. Sefat, R. Jin, M. A. McGuire, B. C. Sales, and D. Mandrus, ^{19}F NMR investigation of the iron pnictide superconductor $LaFeAsO_{0.89}F_{0.11}$, Phys. Rev. B **78**, 100501(R) (2008).

[44] G. Prando, P. Carretta, A. Rigamonti, S. Sanna, A. Palenzona, M. Putti, and M. Tropeano, ^{19}F NMR study of the coupling between $4f$ and itinerant electrons in the pnictide superconductors $SmFeAsO_{1-x}F_x$ ($0.15 \leqslant x \leqslant 0.2$), Phys. Rev. B **81**, 100508(R) (2010).

[45] S. Iimura, S. Matuishi, H. Sato, T. Hanna, Y. Muraba, S. W. Kim, J. E. Kim, M. Takata, and H. Hosono, Two-dome structure in electron-doped iron arsenide superconductors, Nat. Commun. **3**, 943 (2012).

[46] K. Kitagawa, N. Katayama, K. Ohgushi, M. Yoshida, and M. Takigawa, Commensurate itinerant antiferromagnetism in $BaFe_2As_2$: ^{75}As-NMR studies on a self-flux grown single crystal, J. Phys. Soc. Jpn. **77**, 114709 (2008).

[47] S.-H. Baek, H.-J. Grafe, F. Hammerath, M. Fuchs, C. Rudisch, L. Harnagea, S. Aswartham, S. Wurmehl, J. van den Brink, and B. Büchner, ^{75}As NMR-NQR study in superconducting LiFeAs, Eur. Phys. J. B **85**, 159 (2012).

[48] K. Nishiyama, F. Dimmling, Th. Kornrumpf, and D. Riegel, Theory of the Temperature Dependence of the Electric Field Gradient in Noncubic Metals, Phys. Rev. Lett. **37**, 357 (1976).

[49] Q. Huang, J. Zhao, J. W. Lynn, G. F. Chen, J. L. Luo, N. L. Wang, and P. Dai, Doping evolution of antiferromagnetic order and structural distortion in $LaFeAsO_{1-x}F_x$, Phys. Rev. B **78**, 054529 (2008).

[50] N. Qureshi, Y. Drees, J. Werner, S. Wurmehl, C. Hess, R. Klingeler, B. Büchner, M. T. Fernández Díaz, and M. Braden, Crystal and magnetic structure of the oxypnictide superconductor $LaFeAsO_{1-x}F_x$: A neutron-diffraction study, Phys. Rev. B **82**, 184521 (2010).

[51] J. Zhao, Q. Huang, C. de la Cruz, Shiliang Li, J. W. Lynn, Y. Chen, M. A. Green, G. F. Chen, G. Li, Z. Li, J. L. Luo, N. L. Wang, and P. Dai, Structural and magnetic phase diagram of $CeFeAsO_{1-x}F_x$ and its relation to high-temperature superconductivity, Nat. Mater. **7**, 953 (2008).

[52] S. Margadonna, Y. Takabayashi, M. T. McDonald, M. Brunelli, G. Wu, R. H. Liu, X. H. Chen, and K. Prassides, Crystal structure

and phase transitions across the metal-superconductor boundary in the $SmFeAsO_{1-x}F_x$ ($0 \leqslant x \leqslant 0.20$) family, Phys. Rev. B **79**, 014503 (2009).

[53] Y. Luo, Q. Tao, Y. Li, X. Lin, L. Li, G. Cao, Z.-a. Xu, Y. Xue, H. Kaneko, A. V. Savinkov, H. Suzuki, C. Fang, and J. Hu, Evidence of magnetically driven structural phase transition in RFeAsO (R = La, Sm, Gd, and Tb): A low-temperature x-ray diffraction study, Phys. Rev. B **80**, 224511 (2009).

[54] A. Martinelli, A. Palenzona, M. Tropeano, M. Putti, C. Ferdeghini, G. Profeta, and E. Emerich, Retention of the Tetragonal to Orthorhombic Structural Transition in F-substituted SmFeAsO: A New Phase Diagram for $SmFeAs(O_{1-x}F_x)$, Phys. Rev. Lett. **106**, 227001 (2011).

[55] H. Frisch, E. Sonnenblick, V. Vyssotsky, and J. Hammersley, Critical percolation probabilities (site problem), Phys. Rev. **124**, 1021 (1961).

[56] M. Sykes and J. Essam, Critical percolation probabilities by series methods, Phys. Rev. **133**, A310 (1964).

[57] M. Newman and R. Ziff, Efficient Monte Carlo Algorithm and High-Precision Results for Percolation, Phys. Rev. Lett. **85**, 4104 (2000).

[58] F. Nitsche, A. Jesche, E. Hieckmann, Th. Doert, and M. Ruck, Structural trends from a consistent set of single-crystal data of RFeAsO (R = La, Ce, Pr, Nd, Sm, Gd, and Tb), Phys. Rev. B **82**, 134514 (2010).

[59] P. Jeglič, J.-W. G. Bos, A. Zorko, M. Brunelli, K. Koch, H. Rosner, S. Margadonna, and D. Arčon, Influence of the Nd $4f$ states on the magnetic behavior and the electric field gradient of the oxypnictides superconductors $NdFeAsO_{1-x}F_x$, Phys. Rev. B **79**, 094515 (2009).

[60] H. Maeter, H. Luetkens, Yu. G. Pashkevich, A. Kwadrin, R. Khasanov, A. Amato, A. A. Gusev, K. V. Lamonova, D. A. Chervinskii, R. Klingeler, C. Hess, G. Behr, B. Büchner, and H.-H. Klauss, Interplay of rare earth and iron magnetism in RFeAsO (R = La, Ce, Pr, and Sm): Muon-spin relaxation study and symmetry analysis, Phys. Rev. B **80**, 094524 (2009).

[61] A. Alfonsov, F. Murányi, V. Kataev, G. Lang, N. Leps, L. Wang, R. Klingeler, A. Kondrat, C. Hess, S. Wurmehl, A. Köhler, G. Behr, S. Hampel, M. Deutschmann, S. Katrych, N. D. Zhigadlo, Z. Bukowski, J. Karpinski, and B. Büchner, High-field electron spin resonance spectroscopy study of $GdFeAsO_{1-x}F_x$ superconductors, Phys. Rev. B **83**, 094526 (2011).

[62] U. Stockert, N. Leps, L. Wang, G. Behr, S. Wurmehl, B. Büchner, and R. Klingeler, Pr magnetism and its interplay with the Fe spin-density wave in $PrFeAsO_{1-x}F_x$ (x = 0, 0.15), Phys. Rev. B **86**, 144407 (2012).

[63] C. Fang, H. Yao, W.-F. Tsai, J. P. Hu, and S. A. Kivelson, Theory of electron nematic order in LaFeAsO, Phys. Rev. B **77**, 224509 (2008).

[64] M. Ramazanoglu, J. Lamsal, G. S. Tucker, J.-Q. Yan, S. Calder, T. Guidi, T. Perring, R. W. McCallum, T. A. Lograsso, A. Kreyssig, A. I. Goldman, and R. J. McQueeney, Two-dimensional magnetic interactions in LaFeAsO, Phys. Rev. B **87**, 140509(R) (2013).

[65] C. Yasuda, S. Todo, K. Hukushima, F. Alet, M. Keller, M. Troyer, and H. Takayama, Néel Temperature of Quasi-Low-Dimensional Heisenberg Antiferromagnets, Phys. Rev. Lett. **94**, 217201 (2005).

[66] P. Bonfà, P. Carretta, S. Sanna, G. Lamura, G. Prando, A. Martinelli, A. Palenzona, M. Tropeano, M. Putti, and R. De Renzi, Magnetic properties of spin-diluted iron pnictides from μSR and NMR in $LaFe_{1-x}Ru_xAsO$, Phys. Rev. B **85**, 054518 (2012).

[67] S. Sanna, P. Carretta, P. Bonfà, G. Prando, G. Allodi, R. De Renzi, T. Shiroka, G. Lamura, A. Martinelli, and M. Putti, Correlated Trends of Coexisting Magnetism and Superconductivity In Optimally Electron-Doped Oxypnictides, Phys. Rev. Lett. **107**, 227003 (2011).

[68] Y. Yiu, P. Bonfà, S. Sanna, R. De Renzi, P. Carretta, M. A. McGuire, A. Huq, and S. E. Nagler, Tuning the magnetic and structural phase transitions of PrFeAsO via Fe/Ru spin dilution, Phys. Rev. B **90**, 064515 (2014).

[69] K. Malarz and S. Galam, Square-lattice site percolation at increasing ranges of neighbor bonds, Phys. Rev. E **71**, 016125 (2005).

[70] A. Iadecola, B. Joseph, L. Simonelli, L. Maugeri, M. Fratini, A. Martinelli, A. Palenzona, M. Putti, and N. L. Saini, Effect of Ru substitution on atomic displacements in the layered $SmFe_{1-x}Ru_xAsO_{0.85}F_{0.15}$ superconductor, Phys. Rev. B **85**, 214530 (2012).

[71] B. Joseph, A. Iadecola, L. Simonelli, L. Maugeri, A. Martinelli, A. Palenzona, M. Putti, and N. L. Saini, Temperature dependent local atomic displacements in Ru substituted $SmFe_{1-x}Ru_xAsO_{0.85}F_{0.15}$ superconductors, Supercond. Sci. Technol. **26**, 065005 (2013).

[72] A. Martinelli, A. Palenzona, I. Pallecchi, C. Ferdeghini, M. Putti, S. Sanna, C. Curfs, and C. Ritter, Structural properties and phase diagram of the $La(Fe_{1-x}Ru_x)AsO$ system, J. Phys.: Condens. Matter **25**, 395701 (2013).

[73] L. Simonelli, A. Al Zein, M. Moretti Sala, B. Joseph, A. Iadecola, M. Bendele, A. Martinelli, A. Palenzona, M. Putti, G. Monaco, and N. L. Saini, Study of the electronic and magnetic properties as a function of isoelectronic substitution in $SmFe_{1-x}Ru_xAsO_{0.85}F_{0.15}$, J. Phys.: Condens. Matter **26**, 065701 (2014).

[74] A. Martinelli, A. Palenzona, C. Ferdeghini, M. Mazzani, P. Bonfà, and G. Allodi, Pair distribution function analysis of $La(Fe_{1-x}Ru_x)AsO$ compounds, J. Solid State Chem. **220**, 37 (2014).

[75] M. Tropeano, M. R. Cimberle, C. Ferdeghini, G. Lamura, A. Martinelli, A. Palenzona, I. Pallecchi, A. Sala, I. Sheikin, F. Bernardini, M. Monni, S. Massidda, and M. Putti, Isoelectronic Ru substitution at the iron site in $SmFe_{1-x}Ru_xAsO_{0.85}F_{0.15}$ and its effects on structural, superconducting, and normal-state properties, Phys. Rev. B **81**, 184504 (2010).

[76] M. Mazzani, P. Bonfà, G. Allodi, S. Sanna, A. Martinelli, A. Palenzona, P. Manfrinetti, M. Putti, and R. De Renzi, ^{75}As NQR signature of the isoelectronic nature of ruthenium for iron substitution in $LaFe_{1-x}Ru_x$ AsO, Phys. Status Solidi B **251**, 974 (2014).

[77] M. Fu, D. A. Torchetti, T. Imai, F. L. Ning, J.-Q. Yan, and A. S. Sefat, NMR Search for the Spin Nematic State in a LaFeAsO Single Crystal, Phys. Rev. Lett. **109**, 247001 (2012).

[78] Q. Zhang, R. M. Fernandes, J. Lamsal, J. Yan, S. Chi, G. S. Tucker, D. K. Pratt, J. W. Lynn, R. W. McCallum, P. C. Canfield, T. A. Lograsso, A. I. Goldman, D. Vaknin, and R. J. McQueeney, Neutron-Scattering Measurements of Spin Excitations in LaFeAsO and $Ba(Fe_{0.953}Co_{0.047})_2As_2$: Evidence for a Sharp Enhancement of Spin Fluctuations by Nematic Order, Phys. Rev. Lett. **114**, 057001 (2015).

[79] R. T. Gordon, H. Kim, N. Salovich, R. W. Giannetta, R. M. Fernandes, V. G. Kogan, T. Prozorov, S. L. Bud'ko, P. C. Canfield, M. A. Tanatar, and R. Prozorov, Doping evolution of the absolute value of the London penetration depth and superfluid density in single crystals of $Ba(Fe_{1-x}Co_x)_2As_2$, Phys. Rev. B **82**, 054507 (2010).

[80] H. Luetkens, H.-H. Klauss, R. Khasanov, A. Amato, R. Klingeler, I. Hellmann, N. Leps, A. Kondrat, C. Hess, A. Köhler, G. Behr, J. Werner, and B. Büchner, Field and Temperature Dependence of the Superfluid Density in $LaFeAsO_{1-x}F_x$ Superconductors: A Muon Spin Relaxation Study, Phys. Rev. Lett. **101**, 097009 (2008).

[81] A. Shengelaya, R. Khasanov, D. G. Eshchenko, D. Di Castro, I. M. Savić, M. S. Park, K. H. Kim, S.-I. Lee, K. A. Müller, and H. Keller, Muon-Spin-Rotation Measurements of the Penetration Depth of the Infinite-Layer Electron-Doped $Sr_{0.9}La_{0.1}CuO_2$ Cuprate Superconductor, Phys. Rev. Lett. **94**, 127001 (2005).

[82] Y. J. Uemura, L. P. Le, G. M. Luke, B. J. Sternlieb, W. D. Wu, J. H. Brewer, T. M. Riseman, C. L. Seaman, M. B. Maple, M. Ishikawa *et al.*, Basic Similarities Among Cuprate, Bismuthate, Organic, Chevrel-Phase, and Heavy-Fermion Superconductors Shown by Penetration-Depth Measurements, Phys. Rev. Lett. **66**, 2665 (1991).

[83] Y. J. Uemura, V. J. Emery, A. R. Moodenbaugh, M. Suenaga, D. C. Johnston, A. J. Jacobson, J. T. Lewandowski, J. H. Brewer, R. F. Kiefl, S. R. Kreitzman, G. M. Luke, T. Riseman, C. E. Stronach, W. J. Kossler, J. R. Kempton, X. H. Yu, D. Opie, and H. E. Schone, Systematic variation of magnetic-field penetration depth in high-T_c superconductors studied by muon-spin relaxation, Phys. Rev. B **38**, 909(R) (1988).

[84] I. Bozovic, G. Logvenov, M. Verhoeven, P. Caputo, E. Goldobin, and M. Beasley, Giant Proximity Effect in Cuprate Superconductors, Phys. Rev. Lett. **93**, 157002 (2004).

[85] T. Kirzhner and G. Koren, Pairing and the phase diagram of the normal coherence length $\xi_N(T,x)$ above T_c of $La_{2-x}Sr_xCuO_4$ thin films probed by the Josephson effect, Sci. Rep. **4**, 6244 (2014).

[86] Y. Tanabe, K. K. Huynh, S. Heguri, G. Mu, T. Urata, J. Xu, R. Nouchi, N. Mitoma, and K. Tanigaki, Coexistence of Dirac-cone states and superconductivity in iron pnictide $Ba(Fe_{1-x}Ru_x\ As)_2$, Phys. Rev. B **84**, 100508(R) (2011).

[87] A. Sefat, M. McGuire, B. Sales, R. Jin, J. Howe, and D. Mandrus, Electronic correlations in the superconductor $LaFeAsO_{0.89}F_{0.11}$ with low carrier density, Phys. Rev. B **77**, 174503 (2008).

[88] I. Pallecchi, C. Fanciulli, M. Tropeano, A. Palenzona, M. Ferretti, A. Malagoli, A. Martinelli, I. Sheikin, M. Putti, and C. Ferdeghini, Upper critical field and fluctuation conductivity in the critical regime of doped SmFeAsO, Phys. Rev. B **79**, 104515 (2009).

[89] G. Lamura, T. Shiroka, P. Bonfà, S. Sanna, R. De Renzi, F. Caglieris, M. R. Cimberle, S. Iimura, H. Hosono, and M. Putti, Crossover between magnetism and superconductivity in LaFeAsO with low H-doping level, J. Phys.: Condens. Matter **26**, 295701 (2014).

[90] R. S. Gonnelli, D. Daghero, M. Tortello, G. A. Ummarino, V. A. Stepanov, J. S. Kim, and R. K. Kremer, Coexistence of two order parameters and a pseudogaplike feature in the iron-based superconductor $LaFeAsO_{1-x}F_x$, Phys. Rev. B **79**, 184526 (2009).

[91] A. Kondrat, G. Behr, B. Büchner, and C. Hess, Unusual Nernst effect and spin density wave precursors in superconducting $LaFeAsO_{1-x}F_x$, Phys. Rev. B **83**, 092507 (2011).

[92] N. Y. Panarina, Y. I. Talanov, T. S. Shaposhnikova, N. R. Beysengulov, E. Vavilova, G. Behr, A. Kondrat, C. Hess, N. Leps, S. Wurmehl, R. Klingeler, V. Kataev, and B. Büchner, Pinning effects in ceramic $SmO_{1-x}F_x$ FeAs as revealed by microwave absorption, Phys. Rev. B **81**, 224509 (2010).

[93] Y. Kohama, Y. Kamihara, S. A. Baily, L. Civale, S. C. Riggs, F. F. Balakirev, T. Atake, M. Jaime, M. Hirano, and H. Hosono, Doping dependence of the upper critical field and Hall resistivity of $LaFeAsO_{1-x}F_x$ ($x = 0$, 0.025, 0.05, 0.07, 0.11, and 0.14), Phys. Rev. B **79**, 144527 (2009).

[94] C.-C. Lee, W.-G. Yin, and W. Ku, Ferro-Orbital Order and Strong Magnetic Anisotropy in the Parent Compounds of Iron-Pnictide Superconductors, Phys. Rev. Lett. **103**, 267001 (2009).

[95] Q. Luo, D.-X. Yao, A. Moreo, and E. Dagotto, Charge stripes in the two-orbital Hubbard model for iron pnictides, Phys. Rev. B **83**, 174513 (2011).

[96] T. Misawa and M. Imada, Superconductivity and its mechanism in an ab initio model for electron-doped LaFeAsO, Nat. Commun. **5**, 5738 (2014).

[97] N. Fujiwara, S. Tsutsumi, S. Iimura, S. Matsuishi, H. Hosono, Y. Yamakawa, and H. Kontani, Detection of Antiferromagnetic Ordering in Heavily Doped $LaFeAsO_{1-x}H_x$ Pnictide Superconductors Using Nuclear-Magnetic-Resonance Techniques, Phys. Rev. Lett. **111**, 097002 (2013).

[98] J. Yang, R. Zhou, L.-L. Wei, H.-X. Yang, J.-Q. Li, Z.-X. Zhao, and G.-Q. Zheng, New superconductivity dome in $LaFeAsO_{1-x}F_x$ accompanied by structural transition, Chin. Phys. Lett. **32**, 107401 (2015).

[99] M. A. McGuire, D. J. Singh, A. S. Sefat, B. C. Sales, and D. Mandrus, Suppression of spin density wave by isoelectronic substitution in $PrFe_{1-x}Ru_x$ AsO, J. Solid State Chem. **182**, 2326 (2009).